Chinese Chemical Letters 34 (2023) 107841

Contents lists available at ScienceDirect

Chinese Chemical Letters

journal homepage: www.elsevier.com/locate/cclet

Structure-activity relationship of defective electrocatalysts for nitrogen fixation

Yusheng Wang[1], Nan Yang[1], Xue Xin, Yingjie Yu, Yuao Wei, Baoli Zha, Wenjing Liu*

Key Laboratory of Flexible Electronics (KLOFE) & Institute of Advanced Materials (IAM), Nanjing Tech University, Nanjing 211816, China

ARTICLE INFO

Article history:
Received 8 August 2022
Revised 2 September 2022
Accepted 20 September 2022
Available online 23 September 2022

Keywords:
Nitrogen reduction reaction
Defect
Approaches to induce defects
Electrochemistry

ABSTRACT

Ammonia (NH_3), as an important chemical substance and clean energy carrier, plays an indispensable role in industrial and agricultural production. The electrocatalytic synthesis of NH_3 under mild conditions has attracted worldwide attention in the energy field due to its environmental friendliness and cost efficiency, but unsatisfactory NH_3 yields and Faradaic efficiencies are restricting its development. The introduction of defect has been demonstrated as a feasible way to overcome the disadvantages of electrochemistry, as it can regulate the electronic structure and modulate coordination environment of electrocatalysts, which further create active sites and enhance nitrogen adsorption. In this regard, it is necessary to understand the effects of various types of defects on electrocatalysts based on the latest progress in the defect engineering for nitrogen reduction reaction (NRR). In this review, the concept, classifications, and characterization of defects as well as the approaches to create them in electrocatalysts are firstly discussed. Then, certain types of defects (vacancy, dopant, amorphism, edge/corner, and porousness) affecting the performances of various electrocatalysts are further described. Finally, the summary and challenges of electrocatalytic ammonia synthesis are proposed to design advanced electrocatalysts with high efficiency.

1. Introduction

Ammonia (NH_3) is not only a basic chemical used as fertilizer in agricultural production, but also an important chemical composition used in chemical production such as refrigerants and explosives [1,2]. More than 80% of the ammonia is obtained by Haber-Bosch reaction which requires both high temperature and high pressure [3]. In addition, this reaction consumes energy which accounts for about 1% of the world's annual energy consumption and is not conducive to environmental protection and sustainable economic development [4]. Moreover, most of the hydrogen sources for ammonia synthesis are obtained through multi-step reaction of natural gas, resulting in a large amount of carbon dioxide emissions [5]. Considering these problems of energy consumption and gas emission, it is meaningful to design eco-friendly and low-carbon methods for synthesizing ammonia to enhance N_2 fixation under mild conditions [6,7].

So far, some methods such as nitrogenase enzymes technology [8], photocatalysis [9] and plasma technology [10] have been explored for nitrogen fixation under mild conditions. For example, Brown *et al.* used nanocrystalline CdS as photosensitizer to realize the nitrogen fixation by driving MoFe protein to synthesize ammonia simulating the biological nitrogen fixation process [8]. In terms of photocatalytic synthesis of ammonia, Feng *et al.* have recently synthesized novel surface oxygen vacancies (OVs) modified $Bi_2O_2CO_3$ (BOC/OVs) with micronanosheet structure which exhibited good performance in photocatalytic NRR [11]. Plasma-assisted technology involving plasma reactor has been considered as a fast and convenient method to realize the collection of ammonia at ambient conditions, but its development is hindered by the unsatisfactory efficiency [12]. Therefore, it is still necessary to explore new nitrogen fixation technologies with high efficiency and high ammonia yield [1,13].

In recent years, the electrocatalytic synthesis of ammonia by utilizing water as the hydrogen source under ambient temperature and pressure has received unprecedented attention [14]. By this means, it is convenient to use renewable electricity in a distributed way for NRR through mature fuel cells and water electrolyzer technology. However, the N_2 molecule not only possess a strong non-polar N≡N triple bond and the high ionization energy (940.95 kJ/mol), but also the absence of permanent dipoles in its molecules leads to a low proton affinity (493.8 kJ/mol), making hydrogenation of N_2 becomes a challenge [15]. Electrocatalytic reduction of nitrogen to ammonia is a multi-step reaction, which in-

* Corresponding author.
E-mail address: iamwjliu@njtech.edu.cn (W. Liu).
[1] These authors contributed equally to this work.

https://doi.org/10.1016/j.cclet.2022.107841
1001-8417/

volves the transfer of six electrons and six protons. The equilibrium potential of nitrogen and hydrogen evolution reaction (HER) at acid conditions during electrocatalytic reduction is as follows [16]:

$$N_2(g) + 6H^+(aq) + 6e^- \rightleftharpoons 2NH_3(aq)\ E_0 = 0.092\,V\ vs.\ RHE \quad (1)$$

$$2H^+(aq) + 2e^- \rightleftharpoons H_2(g)\ E_1 = 0.000\,V\ vs.\ RHE \quad (2)$$

The potentials of these two equilibrium reactions, Eqs. 1 and 2, are similar. In principle, when a fairly negative potential is applied to the electrode, the N_2 reduction reaction would happen at room temperature and atmospheric pressure [16]. Compared with the potential E_1 of two electrons transfer in hydrogen evolution reaction, E_0 of nitrogen reduction to ammonia represents the average value of multiple steps in this process [17]. Therefore, in the actual electrocatalytic reaction, hydrogen evolution reaction will dominate and lead to a low Faradaic efficiency (FE) [18]. When the current density is very low, there will be a relatively high FE and consequently low ammonia production rate [19]. As a result, designing high-efficient, high-active and high-selective electrocatalysts to enhance the nitrogen fixation with high ammonia yield and FE is desirable [20].

Defect engineering, through precisely controlling the defect features (concentration, morphology, size, *etc.*), can affect the performance of electrocatalysts [21,22]. The advantages of such strategy are as follows: (1) The electrocatalysts with larger surface areas can be obtained by creating defects or modifying the shape structure to speed up electron transfer from the electrode to the reaction interface to further accelerate the electrocatalytic reaction rates [23–25]. For example, Wang *et al.* [26] fabricated porous gold film (pAu/NF) directly loaded on nickel foam as electrocatalysts. The three-dimensional porous structure of pAu/NF possesses a large specific surface area and abundant active sites to enhance the adsorption of nitrogen and accelerate the electron and proton transfer in the catalytic reaction, thus greatly enhancing the catalytic performance of the reaction. (2) The introduction of doping heteroatoms or vacancies on the surface of catalysts could adjust the electron density of active sites to increase the nitrogen adsorption capacity and effectively reduce the overpotential during the catalytic process [27]. For example, Fan *et al.* [28] achieved the crystalline phase transition of Mo_2C from hexagonal to cubic by B doping into Mo_2C phase. The B-doped cubic Mo_2C has stronger hybridization with the 2p orbitals of the active adsorbed nitrogen atom in the density state near the Fermi energy level, which indicates that the B doping enhances the bonding between the catalytic material and the reacting species, thus favoring the stabilization of the adsorbed species and lowering the NRR reaction energy barrier. In this review, we summarize the latest progress about the applications of defects in the electrocatalytic synthesis of ammonia under mild conditions. We first introduce the concept, classifications and characterization of defects. Secondly, the approaches of introducing defects into various electrocatalytic nanomaterials are analyzed. Thirdly, a summary of these defects commonly used in NRR is provided. These defects are divided into five types (vacancy, dopant, amorphism, edge/corner, and porousness) and their influence on the performances of the electrocatalysts is explained in detail (Scheme 1). Finally, our points of view on challenges and outlook in the development of NRR electrocatalysts are proposed.

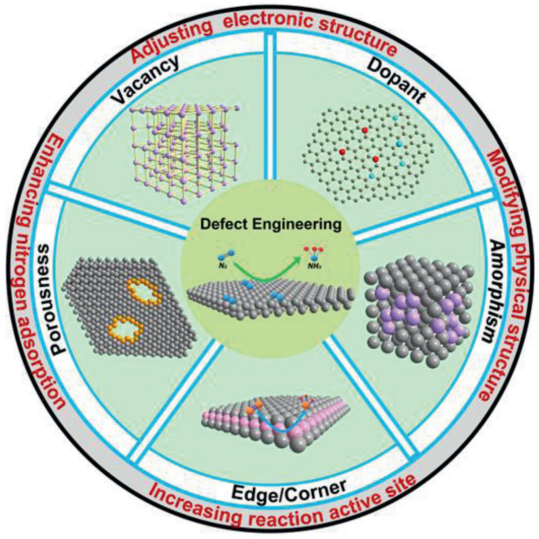

Scheme 1. Schematic diagram of defects engineering for NRR (vacancy, dopant, amorphism, edge/corner, and porousness). The advantages of defects towards NRR can be summarized into the following four points: (1) adjusting electronic structure; (2) modifying physical structure; (3) increasing reaction active site; and (4) enhancing nitrogen adsorption.

2. Defects

2.1. Defect concept

Defects play an important role in tuning the electronic states of electrocatalysts and enhancing reaction active sites, influencing the performances of electrocatalysts. Therefore, it is necessary to understand the definition of defects and classify the synthetic routes to create them. The term "defect" is generally defined as the distortion of periodic potential filed in crystal lattice structure [29]. According to the definition of geometry, defects are commonly divided into point defects, line defects, plane defects, and bulk defects, which fall into the category of zero-dimensional (0D), one-dimensional (1D), two-dimensional (2D) and three-dimensional (3D) defects, respectively [30,31]. The creation of defects in the catalysts depends on external conditions, synthetic methods or post-treatment methods, *etc.*

2.2. Classifications

Among the reported defect catalysts affecting NRR electrocatalytic activity, the defect species could be divided into vacancies, dopants, amorphisms, edges/corners, and porousness.

Vacancies are formed because the lattice atoms at the lattice nodes break free from the binding of the surrounding atoms and deviate from the original position, thus changing the physicochemical properties of crystal materials. These atomic scale defects can be intrinsic or introduced into the surface of catalytic materials, which can effectively enhance the catalytic activity. For example, anion vacancy, especially OVs on metal oxide electrocatalyst have been widely reported, including MnO_2 [32], $NiCo_2O_4$ [33], CeO_2 [34] and TiO_2 [35], which have been proven to be efficient active sites for the adsorption and activation of reactants. Consistent with the OVs, other anionic electrocatalysts such as nitrogen vacancies for Ni_3N [36], g-C_3N_4 [37], and sulfur vacancies for CoS@FeS [38], CdS [39], and cationic vacancies in electrocatalytic materials such as iron vacancies [40], molybdenum vacancies [41] and copper vacancies [42] have also been reported with reliable performances.

Heteroatom doping is formed by introducing foreign atoms [43]. Foreign atoms enter the lattice to either replace the original atoms into the normal lattice points, or occupy interstitial positions where there are no atoms. According to the different types of dopants, they can be divided into metal doping, such as Cu [44], Co [45], Ru [46] and non-metal doping such as N [47], P [48] and B [49]. In addition, the direct confinement of atoms or ions in the crystal lattice is also a type of doping. Ma *et al.* [50] designed atomic Pt catalysts with crystal lattice confinement in metal carbides and demonstrated that the confined atoms exhibited

near-zero valence states and matched metal Pt electronic structure, thus providing a catalytic behavior similar to that of metal Pt adsorbed on *H on the surface of metal Pt, which is much better than that of Pt sites adsorbed on WC_x. This provides a new idea for NRR to effectively improve the activation and adsorption of N_2. In general, dopants can not only adjust the electron density distribution around active sites, but also may lead to structure transformation to improve the activity of electrocatalysts [51–54].

Amorphism refers to materials lacking the characteristics of long-range order and periodicity. The accumulation of vacancies or doping defects may produce disordered crystal structure with exposed active sites, which can enhance the transport ability of electrons and protons during the catalytic process. Some recent reports show that amorphous catalysts have advantages in catalytic performance over crystalline catalysts such as Ni-P alloy [55] and NiO_x-C [56], possibly due to their long-range disordered structure and abundant unsaturated active sites.

The edge and corner atoms of nanocrystals possess high surface energy and activity due to the presence of unsaturated coordination bonds, which have been shown to significantly reduce the activation energy barriers of inert molecules such as N_2 [57,58]. For example, the edge defects of catalysts such as MoS_2 [59] and MXene [60] are demonstrated to tune electron density, which further enhances their electrocatalytic performance. Porous structures are usually caused by the loss of templates or metastable surface atoms during the post-synthesis of catalytic nanomaterials (pyrolysis, reduction, etching, *etc.*), which may not only provide abundant active sites but also enhance the enrichment of N_2 and intermediates, prolong N_2 residence time, accelerate the transformation of specific species, and shorten the electron transport path [61]. In summary, the defect sites have the ability to change the coordination environment and charge distribution of surrounding atoms, thus regulating the adsorption capacity of key intermediates, and further affecting the electrocatalytic activity.

2.3. Characterizations

The characterization of defects at the atomic level is still challenging. Some advanced characterization techniques have been developed to understand the existence species and formation mechanism of defects. High angle annular dark field scanning transmission electron microscope (HAADF-TEM) can be used for visual defect detection. As shown in Figs. 1a and b, the white dot [62] and black hole [63] represent the existence of metal vacancies and doping sites, respectively, because the imaging intensity is proportional to the square of the atomic number. Other defects such as twin boundaries can also be captured (Fig. 1c) [64]. X-ray photoelectron spectroscopy (XPS), as an effective non-destructive surface measurement technology, can well display the electronic effect caused by surface defects through the shift of binding energy. As shown in Fig. 1d, the Rh 3d peak of a/c-Rh shifts slightly to a higher binding energy due to the existence of disordered atoms in the amorphous state [65]. Electron paramagnetic resonance (EPR) advances in detecting unpaired electrons, thus becoming an effective method to characterize vacancies. For instance, $CoMnNiO_x$-S-A shows stronger EPR signal at $g = 2.003$ than that of $CoMnNiO_x$-S indicating that rich OVs have been introduced into $CoMnNiO_x$-S-A (Fig. 1e) [66]. Transient photoluminescence (PL) spectroscopy can qualitatively detect the vacancy concentration produced by photon exciton. For example, NbO_x exhibits stronger photoluminescence intensity at 588 nm than Nb_2O_5, indicating its higher OVs concentration (Fig. 1f) [67]. X-ray diffraction (XRD) is also an effective method to define the crystal structure and change the law of catalytic materials. Usually, there are obvious peaks in the diffraction pattern of crystalline materials, while large envelope peaks in that of amorphous materials (Fig. 1g) [68]. Positron annihilation spectroscopy (PAS) provides direct information about the types and relative concentrations of defects and is a powerful technique for studying defects in materials. For instance, Liu *et al.* employed PAS to identify defect changes in $CoSe_2$ nanosheets, with the distinct lifetime and intensity being slightly extended in Fig. 1h. This suggested improved defect dimension and content compared with $CoSe_2$ solid materials [69]. X-ray absorption spectroscopy (XAS) including X-ray absorption near edge structures (XANES) and extended X-ray absorption fine structures (EXAFS) has been generally used to characterize the electronic and geometric structures of defects at the atomic scale. For example, by utilizing EXAFS spectra, Li *et al.* reported that atomically dispersed Fe atoms interact with N through coordination bonds (Fig. 1i) [70].

In summary, different types of defects can be obtained by controlling some conditional factors *via* various approaches and have been proven to improve electrocatalysts' performances [71]. In the following sections, popular methods about how to introduce defects, for example, by etching with different etchants, by using plasma technology at different atmospheres and plasma concentrations and by pyrolyzing catalysts under different temperatures and pressures, will be introduced in detail.

2.4. Approaches to induce defects

2.4.1. Etching

Etching is a technology that removes materials by chemical reaction or physical impact, which is generally considered to be an effective and direct approach to induce defects on nanoparticles [72]. Various etching approaches (chemical etching, base etching, acid etching and plasma etching) have been developed in a more facile and convenient way, enabling a deliberate control over the concentrations and types of defects in electrocatalysts for NRR.

As a well-known approach, chemical etching introduces etching agent to react with the catalysts and obtain target materials. The etchants such as halide ions and oxygen are commonly used in the preparation of precious metal catalysts [73]. For example, Wang *et al.* reported Pt_3Sn catalyst with rich defects for formic acid oxidation utilizing chloridion and oxygen as etchants, platinum acetylacetonate ($Pt(acac)_2$), $SnCl_2{\cdot}2H_2O$, polyvinylpyrrolidone (PVP), and *N*,*N*-dimethylformamide (DMF) as reagents at high temperature and high pressure. With the increase of precursor concentration, the reduced Sn was diffused into the lattice of Pt due to the existence of high heat energy, and thus a large number of cubic Pt_3Sn nanocubics with rich defects were formed during the reaction [74]. Furthermore, Xia *et al.* synthesized Pt-based icosahedral nanocages with twin boundaries defects by chemical etching $Pd@Pt_{4.5\,L}$ nanomaterials as precursors for electrocatalytic reactions. The introduction of the etchants $FeCl_3$ and KBr by controlling the etching dose and etching time not only selectively etched Pd out, but also increased the surface area of the material and the abundance of three-phase boundary [75]. As a result, the as-synthesized Pt icosahedral nanotubes had a better electrocatalytic performance than commercial Pt/C catalyst due to the existence of large surface, twin boundaries and {111} facets.

Alkali etching and acid etching are relatively facile methods by introducing base or acid for inducing defects. In terms of alkali etching, Zhu *et al.* found a new nanomaterial with rich-carbon pentagonal defects (PD-C), whose precursor was prepared by pouring potassium hydroxide solution into fullerene suspension (Fig. 2a) [76]. Density functional theory (DFT) and experiments have proven that the inherent pentagonal defects of carbon nanomaterials can be used in electrocatalysis due to the good electrochemical reaction activity, strong oxygen binding ability and stability. MXene is a two-dimensional inorganic nanomaterial composed of transition metal carbides, nitrides or carbonitrides, with multiple atomic layer thicknesses, rich components and large specific sur-

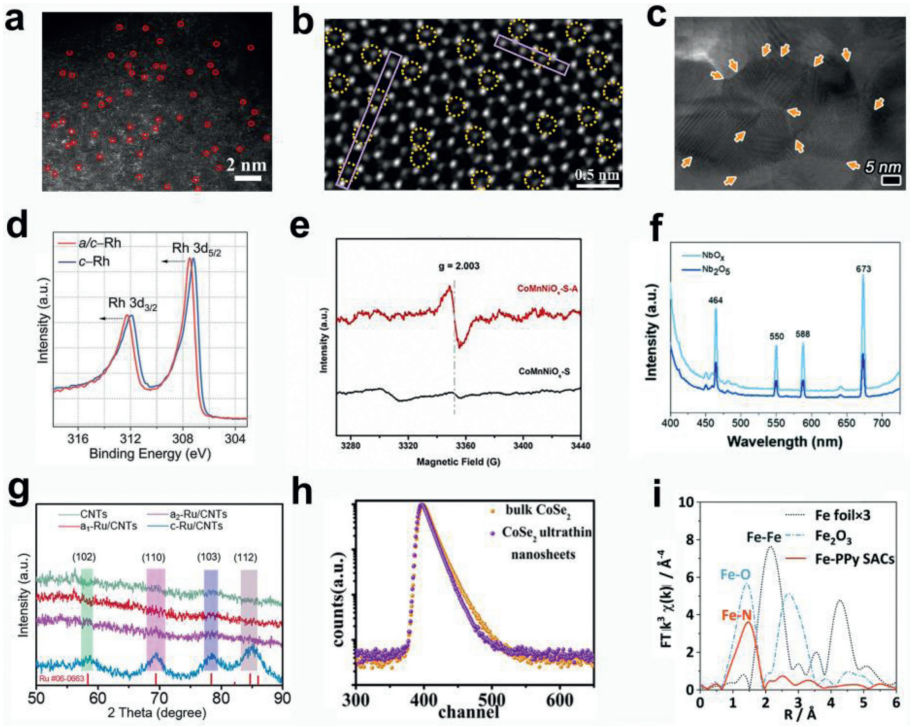

Fig. 1. Characterizations of defects in nanomaterials. (a) HAADF-STEM images of SA-Fe-NHP highlighting isolated Fe atoms. Reproduced with permission [62]. Copyright 2020, John Wiley and Sons. (b) HAADF-STEM images of sulfur vacancies on MoS_2. Reproduced with permission [63]. Copyright 2020, American Chemical Society. (c) HRTEM image of defect rich SnO_2, and the arrows indicate the grain-boundary surface terminations. Reproduced with permission [64]. Copyright 2021, Elsevier. (d) XPS spectra of *a*/*c*-Rh nanosheets (NSs) and *c*-Rh NSs. Reproduced with permission [65]. Copyright 2021, John Wiley and Sons. (e) EPR spectra of $CoMnNiO_x$ with different contents of oxygen vacancies. Reproduced with permission [66]. Copyright 2022, Elsevier. (f) PL spectra of NbO_x and Nb_2O_5. Reproduced with permission [67]. Copyright 2022, Royal Society of Chemistry. (g) XRD patterns of amorphous and crystalline Ru/CNTs catalyst. Reproduced with permission [68]. Copyright 2022, American Chemical Society. (h) Positron lifetime spectra of ultrathin $CoSe_2$ nanosheets and bulk $CoSe_2$. Reproduced with permission [69]. Copyright 2014, American Chemical Society. (i) EXAFS spectra of Fe foil, Fe-PPy and Fe_2O_3 with different doping sites. Reproduced with permission [70]. Copyright 2021, Royal Society of Chemistry.

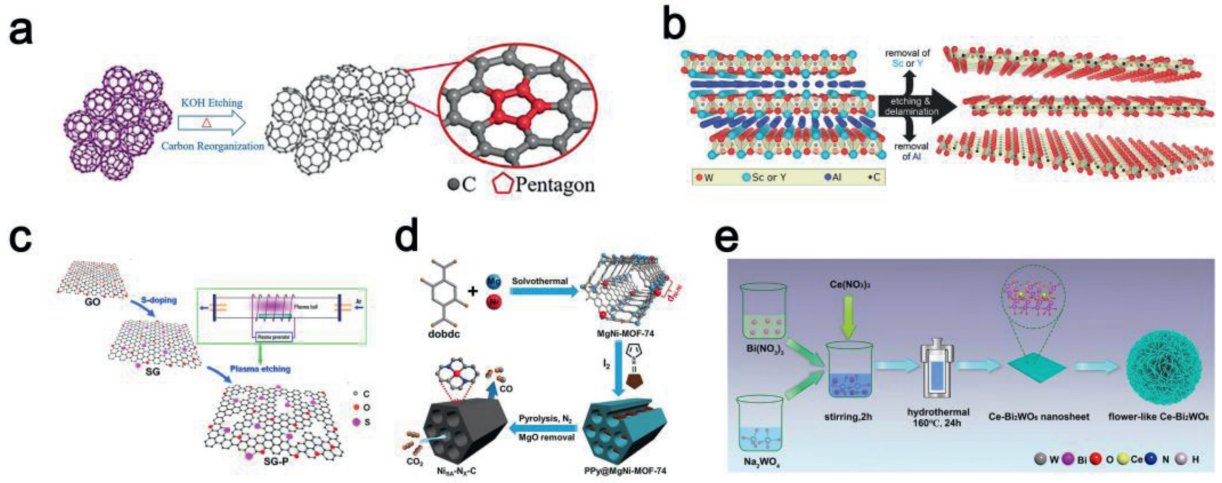

Fig. 2. (a) Illustration of the KOH etching synthetic method of PD-C. Reproduced with permission [76]. Copyright 2019, John Wiley and Sons. (b) $W_{1.33}C$ MXene with ordered vacancies after selective etching and delamination. Reproduced with permission [79]. Copyright 2018, John Wiley and Sons. (c) Schematic illustration of the preparation process of SG-P and the plasma system. Reproduced with permission [83]. Copyright 2017, Elsevier. (d) Schematic illustration of the preparation procedure for Ni-implanted N-doped nanoporous carbons. Reproduced with permission [87]. Copyright 2020, John Wiley and Sons. (e) Synthetic procedure of Ce-Bi_2WO_6. Reproduced with permission [96]. Copyright 2021, American Chemical Society.

face area [77,78]. In terms of using hydrofluoric acid as an etchant, Meshkian *et al.* synthesized the vacancy-rich $W_{1.33}C$ nanosheets by selectively etching away the A(Al) layer and interlayer Sc/Y from $(W_{2/3}M_{1/3})_2AlC$ (M = Sc and Y) nanosheets (Fig. 2b) [79]. Ma *et al.* successfully fixed the defective PdZn nanoparticles on the N-doped hollow carbon polyhedrons (NHCP) as NRR electrocatalysts by etching PdZn/NHCP with sulfuric acid [80]. PdZn/NHCP was synthesized by reacting Pt-based compounds with ZIF-8 during heat treatment. Accordingly, due to the rich exposed defects and porous carbon matrix, the surface area of the catalysts and the electron transport capacity were significantly improved.

Plasma etching, which utilizes the plasma to produce a high energy ionized gas and strong ultraviolet radiation, can be used to create defects by means of ion penetration, covalent bond destruc-

tion, ion impact, *etc.* [81]. After nanomaterials (graphene, metal compounds, *etc.*) were etched, not only abundant active sites can be obtained to increase the surface area of catalysts, but also more channels will be provided on the surface of catalysts to accelerate the mass transport of materials [82]. For example, using plasma etching technology to treat S-doped graphene (SG), Tian *et al.* created a large number of topological defects on graphene. The SG after plasma (SG-P) etching exhibited an obviously improved electrocatalytic activity (Fig. 2c) [83]. In another example, Zhang *et al.* reported a OVs-rich TiN electrocatalyst for NRR by plasma etching under Ar atmosphere for 10 min *via* using modified TiN which was ball milled for 8 h. The etching method exposes abundant vacancies in the material, allowing it to exhibit a higher NRR performance than pure TiN without OVs. Wang *et al.* introduced rich defects on (110) crystal face nanoplates of Bi through the plasma bombardment of Bi_2O_3 in a 30 Mega Hertz Radio Frequency excited quartz tube at a power density of 300 W for about 5 min [30]. Notably, the plasma-treated Bi showed much higher performance than those Bi samples without treatment. These above progresses demonstrate the plasma technology as an effective route to modify the electronic structure of Bi in order to get more (110) crystal faces, thus improving the active site of NRR and enhancing the catalytic performance.

In summary, etching is an effective method to introduce defects in catalysts which is applicable to various kinds of materials (noble metals, transition metals, nonmetals, *etc.*). Chemical etching, alkali etching and acid etching belong to wet-etching, which is an etching method that peels off the etched material through the chemical reaction between the chemical etching solution and the etched material. In contrast, dry etching etches materials mainly by plasma, in which way, the types of defects can be controlled by reasonable selection of gas concentration, atmosphere type, etching time, pressure, *etc.* Generally speaking, the conditions required for etching are relatively mild, rendering possibility of the large-scale production.

2.4.2. Pyrolysis treatment

Pyrolysis treatment is a convenient and rapidly developed technology to introduce rich defects and various vacancies into carbides, nitrides and oxides to enhance the activity of catalysts [84,85]. The precursors such as Metal Organic Frameworks (MOFs), biomass, metal salts and metal free materials under different annealing treatment (*e.g.*, temperature and time) in disparate gas flow (*e.g.*, NH_3, H_2, N_2 and Ar) could create diverse defects in nanostructures [43]. For instance, MOFs are composed of metal ions and organic connecters forming porous structures with the merits of large surface area, adjustable structure and high porosity. MOFs as precursors can be decomposed into more stable conductive carbon/metal based porous materials (such as metal oxide/phosphide) with rich defects by means of pyrolysis treatment [86]. Jiang *et al.* reported a single-atom Ni electrocatalyst by pyrolysis of pre-treated bimetallic precursor MgNi-MOF-74. MgNi-MOF-74 was first introduced with Mg ions to increase the spacing between adjacent Ni atoms. Moreover, the introduction of polypyrrole (PPy) as a ligand could effectively stabilize Ni atoms, and then the ppy@MgNi-MOF-74 was transformed into Ni-implanted N-doped porous carbon through pyrolysis treatment which showed good electrocatalytic activity (Fig. 2d) [87]. Chen *et al.* reported MoFe-phosphorus doped carbon (PC) microspheres with various vacancies as NRR electrocatalysts *via* carbonization of MoFe-MOFs in Ar at 300 °C for 2 h [88]. Another defective electrocatalyst CuPt/NC fabricated by pyrolyzing Cu-tpa MOF along with Pt precursor under Ar-H_2 atmosphere at 700 °C for 3.5 h exhibited highly efficient NRR activity [89]. Huang *et al.* reported N-doped carbon aerogel with large amounts of defects *via* carbonization of zinc 2-methylimidazolate (ZIF-8) in N_2 at 1000 °C for 3 h. Specifically, ZIF-8 precursor was first obtained by solvothermal treatment of Zn ions, and then pyrolyzed with carboxymethylcellulose composite gel (CMCC) to obtain N-doped porous carbon framework, which presented good electrical conductivity, thermal stability and chemical stability [90].

Besides MOF materials, biomass fuel is also a common source of carbon. Bhuvanendran *et al.* prepared a highly efficient active CeO_2 on biochar carbon (CeO_2/BC700) through pyrolyzing CeO_2/BC at 700 °C for 2 h [91]. CeO_2, as a stable rare earth oxide, is not only rich in storage but also capable of transferring electrons, and therefore usually serve as a high-quality supporter to combine with matrix materials in the field of electrocatalysis [92]. The experimental results showed that the doping of nitrogen and phosphorus and the OVs of CeO_2 contributed to high electrocatalytic activity. Moreover, the pyrolysis treatment of metal-free materials is also a common way to introduce defects. For example, Chen *et al.* successfully prepared amorphous carbon based nanosheets (BCN) with B-N substitutions and rich defects by annealing the organic precursors composed of PEG-2000, boric acid, and urea under Ar atmosphere at 900 °C for 2 h [93]. The theoretical and experimental results showed that B-N doping can not only provide the active trigger point and active center, but also effectively inhibit HER in NRR. In this way, more active centers and defects can be obtained by adjusting doping parameters reasonably to produce highly efficient catalysts under the same environmental conditions.

In summary, pyrolysis treatment is a facile approach to anneal different nanomaterials (MOFs, metal compounds, nonmetal compounds, *etc.*) and introduce defects whose parameters (concentration, morphology, types, *etc.*) can be managed by controlling the anneal time, temperature, atmosphere, *etc.* Considering the wide varieties of nanomaterials, more catalysts with rich defects will be prepared *via* pyrolysis treatment for electrocatalytic reaction.

2.4.3. Other alternative approaches

In addition to the approaches described above, there are alternative approaches reported to induce defects such as chemical reduction method, "stacking and carving strategy", hydrothermal method, and Prussian-blue-analogue-sacrificed strategy.

The chemical reduction method adopts reducing agents ($NaBH_4$, or NaH_2PO_4, *etc.*) to reduce the metal ions, at the same time, the B or P and the reduced metals are converted to a monomeric state while precipitating to form an alloy under reducing conditions. This method has the advantage of simple equipment and easy operation, so it is usually used for the synthesis of amorphous alloys such as M-B or M-P (M = Fe, Co, Ni, Ru, *etc.*) and further in the study of electrocatalytic properties. Wang *et al.* [94] reported amorphous $Ni_{0.5}Fe_{0.5}B$ nanosheets by utilizing $NaBH_4$ as the reducing agent to reduce the mixed salt solution of $FeCl_3$ and $NiCl_2$ in one step at room temperature. This amorphous nanosheet exposes abundant vacancies and unsaturated coordination sites to make it exhibit excellent electrocatalytic performance in NRR.

"Stacking and carving strategy", as an ideal approach to improve the performance of catalyst, can introduce defects on Pt-based nanomaterials *via* controlling the carving path and stacking route of crystal growth. In the "stacking" route, the nanoparticles formed *in situ* are arranged regularly in the process of crystal growth, thus resulting in a large number of defects in the junction region. While in the "carving" path, the particles formed *in situ* are etched regularly during the crystal growth process, and a large number of defects are produced in the eroded area. These two routes encouraged Wang's team to synthesize Pt-Fe and Pt-Zn nanoparticles with distinct 3D defects nanostructures [95].

Hydrothermal method is an efficient and common way to prepare defective electrocatalysts. For example, the defective Ce-doped Bi_2WO_6 with nanoflower morphology was synthesized by mixing $Bi(NO_3)_3{\cdot}5H_2O$, Na_2WO_4 and $Ce(NO_3)_3{\cdot}6H_2O$ under Teflon-lined

autoclave at the temperature of 160 °C for 24 h (Fig. 2e) [96]. The as-synthesized catalyst Bi_2WO_6 has the crystal defects, which could facilitate N_2 adsorption and further enhance NRR activity. Polyoxometalate based MOFs (POMOFs) are another typical example of excellent precursors, which combine the excellent redox activity of POMs with the porosity of MOFs [97]. Ma *et al.* achieved an efficient NRR electrocatalyst $Fe_{1.89}Mo_{4.11}O_7/FeS_2$@C by using PMo_{12}@MIL-100(Fe)@PVP as the precursor *via* hydrothermal technique. The high activity during electrocatalytic process came from the formation of Mo-N bond, which could be inclined to adsorb *N-NH and be apart from $*NH_2$ species thus reducing the reaction energy barrier. Manganese oxides are considered as a promising material because of their high abundance.

$KNi[Fe(CN)_6]$ is a Prussian blue compound possessing a rigid and open framework structure and large-sized interstitial channels, which is commonly used as a sacrificial template in the synthesis of catalysts. Recently, *via* template sacrificed strategy, abundant Ni-Fe vacancies with rich-defect cubic nanoflowers (Ni-Fe-$K_{0.23}MnO_2$ CNFs-300) were successfully synthesized by annealing Ni-Fe-doped $K_{0.23}MnO_2$ cubic nanoflowers (Ni-Fe-$K_{0.23}MnO_2$ CNFs) under Ar atmosphere at 180 °C for 2 h. The Ni-Fe-$K_{0.23}MnO_2$ CNFs were obtained by hydrothermal treatment of $KNi[Fe(CN)_6]$, $KMnO_4$ and KCl [98]. Theoretical calculation and experimental data manifested that the catalyst had excellent electrocatalytic performance over water decomposition, possessing much lower overpotential and better durability than other reported manganese oxide based electrocatalysts.

3. Defect types induced in NRR

3.1. Vacancies

The vacancy regulation concept emerges from the design philosophy of "less is more" and offers an opportunity to discover the anonymous quantum phenomenon. The defect fabrication in electrocatalysts with a suitable and well-defined vacancy is a key strategy for further optimizing the catalytic efficiency [99,100]. In addition, the incorporation of vacancies may favorably influence the electronic structure of catalysts, leading to fast charge transfer and optimal effective adsorption of intermediates for electrocatalytic reactions [101]. There are numerous types of vacancies including oxygen [102], sulfur [103], selenium [104] and metal-ion vacancies [63], which can ingeniously adjust the property of the surface adsorption for reaction intermediates thus enhancing the electrocatalytic activity [105].

3.1.1. Oxygen vacancies

OVs, the most prevailing anion vacancy in transition-metal oxides (TMOs) because of their low energy, are extensively accepted as a vital approach to perturb the surface electronic configuration and tailor the intrinsic physicochemical property of oxides [106]. The introduced OVs in TMOs may serve as active sites for the adsorption of reactants and intermediates, thereby decreasing the activation energy barrier and playing a significant role in promoting electrocatalytic reactions [107–111]. Moreover, the metastable electrons can be easily trapped in OVs to relocate to the anti-bonding orbital of N_2 molecule, thus enhancing the cleavage energy of N≡N bond for corresponding catalytic reactions and fostering NRR activity. These attractive properties of OVs ensure their positive role in regulating the activities of various catalytic processes in the electrocatalysis field.

Recently, numerous works have verified that TMOs can be utilized as NRR catalysts, especially with the assistance of OVs [112–119]. As we all know, Fe element plays an indispensable role in the Haber-Bosch process, and therefore Fe-based nanomaterials as well as their derivatives have been extensively investigated as NRR electrocatalysts. Zhang *et al.* proposed a task-specific ionic liquid approach to prepare α-Fe_2O_3 nanocubes with rich OVs for enhanced NRR performance, offering an ammonia yield of 32.13 μg h^{-1} mg_{cat}^{-1} with FE of 6.63% at −0.3 V *vs.* RHE in 0.1 mol/L KOH [118]. Upon the introduction of the ionic liquid *n*-octylammonium formate in the reaction system, the reductant formic anion of ionic liquid *in situ* triggered rich OVs into α-Fe_2O_3 nanocubes. The formation of OVs left lone pair electrons on the surface of the catalyst, prompting the N_2 polarity and enhancing the N_2 activation and adsorption. Therefore, Fe_2O_3 coupled with OVs contributed to the exceptional activity of electrochemical NRR. Inspired by the Fe oxide-based materials, researchers have also studied other TMO-based materials as electrocatalysts for NRR such as MoO_3 nanosheet, Nb_2O_5 nanofiber, multishelled hollow Cr_2O_3 microsphere, and MnO_2 nanoarray, which all manifested potential in electrocatalytic NRR. However, many of these works only focus on selectivity or activity and have not taken the metal oxidation state into consideration. Therefore, it still remains unknown whether the OVs contribute to the activity improvement of NH_3 synthesis or not.

Some other works reported the importance of OVs concentration [103,120]. Han *et al.* tuned the OVs of TiO_2 by controlling the synthetic temperature to study the influence of OVs concentration on NRR activity (Fig. 3a) [120]. At −0.12 V, rich OVs were obtained in anatase TiO_2 with NH_3 yield of about 3.0 μg h^{-1} mg_{cat}^{-1} and FE of 6.5% (Fig. 3b). The pristine and rich OVs structures of TiO_2 were simulated (Fig. 3c), and theoretical calculations further demonstrated the active role of OVs played in promoting the selectivity of nitrogen. The lowest energy reaction pathway was $*N_2 \rightarrow *NNH \rightarrow *NNH_2 \rightarrow *NHNH_2 \rightarrow *NH_2NH_2 \rightarrow *NH_2 + NH_3 \rightarrow *NH_3 + NH_3 \rightarrow 2NH_3$. The first step $*N_2 \rightarrow *NNH$ involved the cleavage of the nitrogen triple bond and the adsorption of hydrogen, and was considered to be a key step in electrolysis. DFT calculations showed that the energy barrier required for the anatase-OVs in the first hydrogenation step was 1.5 eV lower than that of the pristine precursor, indicating that the anatase-OVs can enhance the adsorption capacity of hydrogen and effectively inhibit HER. Thereby, the ammonium yield and Faraday efficiency were further improved (Fig. 3d).

In summary, the OVs existed in electrocatalysts exert a certain effect on bringing high NRR performance. However, it still needs

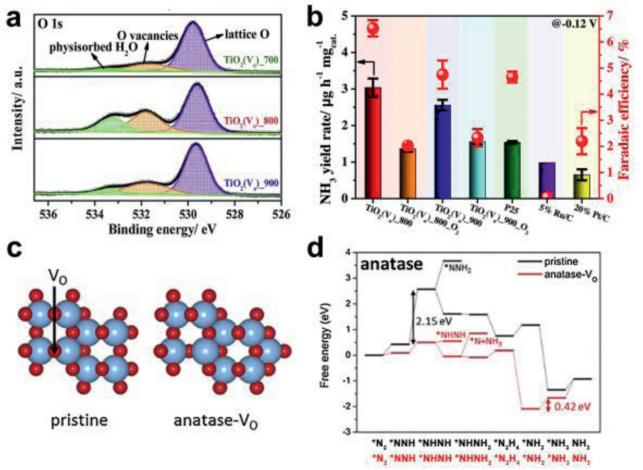

Fig. 3. (a) O 1s XPS spectra of TiO_2 under different temperatures. (b) NH_3 yield rates and FEs of different catalysts at −0.12 V. (c) Optimized geometries (top-view) of pristine and the most stable surface oxygen vacancy containing anatase (101). The sky blue and red balls indicate Ti and O atoms, respectively and the free energy ΔG for NRR is shown in (d). Reproduced with permission [120]. Copyright 2019, Elsevier.

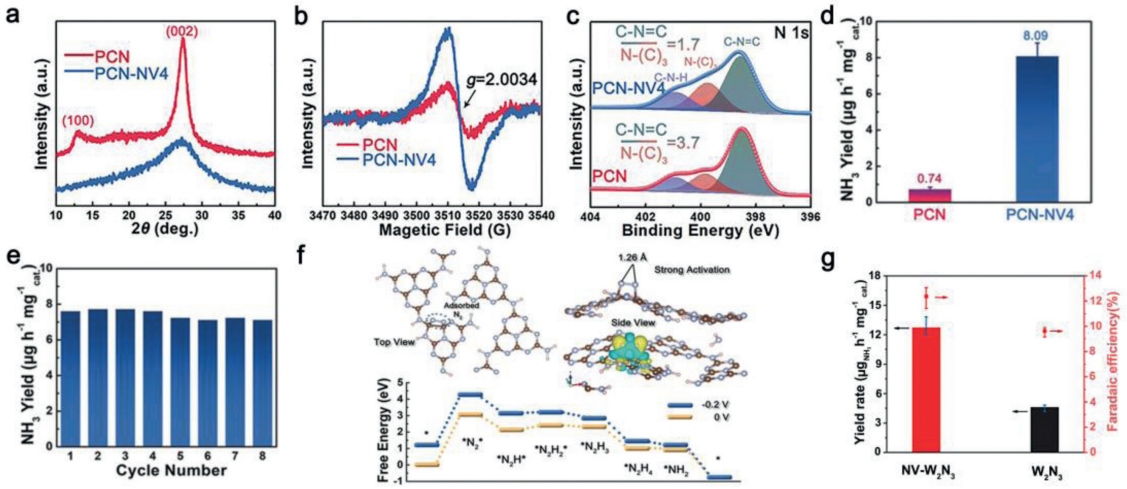

Fig. 4. Characterizations of PCN with and without NVs: (a) XRD patterns and (b) EPR spectra. (c) N 1s XPS spectra. (d) Ammonia yield. (e) Cycling test of PCN-NV. (f) Free energy diagram for NRR on NVs engineered PCN at equilibrium potential. Reproduced with permission [124]. Copyright 2018, John Wiley and Sons. (g) NH_3 yields and FE of NV-W_2N_3 and W_2N_3 at −0.2 V *vs.* RHE. Reproduced with permission [125]. Copyright 2019, John Wiley and Sons.

more explanations to determine the OVs position, the exact electrocatalysts with OVs for excellent NRR performance.

3.1.2. Nitrogen vacancies

Oxygen vacancies as described above can activate N_2 and significantly enhance interfacial electron transfer to boost NRR performance. That tempts us to turn our attention to study other defects. The DFT results of the transition metal nitride (VN, ZrN, NbN and CrN) show that these materials as electrocatalysts are more active towards NRR than towards the competing HER [121–123]. Therefore, the nitrogen vacancies (NVs) are expected to play a critical role in conversing N_2 and adsorbing N_2 molecules, which will in turn enhance the NRR performance.

Lv *et al.* reported experimentally and theoretically that NRR performance could be improved through inducing NVs in the metal-free polymeric carbon nitride (PCN) [124]. Experimentally, NVs were generated inside PCN by pyrolysis under the argon atmosphere and the NVs concentration was regulated by adjusting the calcination condition. XRD patterns revealed a wide and weak peak, indicative of the formation of NVs (Fig. 4a). Observing from the EPR spectra, a strong signal at $g = 2.0034$ was detected, which was related to an unpaired electron owing to the existence of NVs (Fig. 4b). Fourier transform infrared spectroscopy and XPS (Fig. 4c) have been used to identify the exact location of the NVs in the PCN. The resulting catalyst, PCN-NV, exhibited superior electrocatalytic NRR performance with reasonable NH_3 rate of 8.09 μg h^{-1} $mg_{cat}{}^{-1}$ and FE of 11.59%, nearly over 10-fold enhancement in comparison to pristine PCN (Fig. 4d). This exceptional performance revealed that the enrichment of NVs boosted the NRR electrocatalysis. Cycling tests proved that PCN-NV was stable during the electrochemical NRR process (Fig. 4e). DFT revealed that dinitrogen molecules might be chemisorbed to PCN by building a binuclear end-on bound structure for the transformation of spatial electrons, and NRR adopted an alternative associative pathway (Fig. 4f).

Besides the metal-free catalysts, Jin *et al.* successfully synthesized a new ultrathin 2D layered W_2N_3 with surface NVs for electrochemical NRR [125]. Computational studies proposed that NVs on W_2N_3 could produce an electron-deficient environment that would enable nitrogen adsorption and diminish the thermodynamic potential of NRR. The activity and stability of NVs were estimated by electrochemical measurements and various *ex-situ* characterizations. The NVs-engineered 2D W_2N_3 achieved a higher NRR performance with an average NH_3 formation rate of 11.66 ± 0.98 μg h^{-1} $mg_{cat}{}^{-1}$ ($3.80 \pm 0.32 \times 10^{-11}$ mol cm^{-2} s^{-1}) and FE of 11.67% ± 0.93% at −0.2 V *vs.* RHE than that of pristine W_2N_3 (Fig. 4g). Nuclear magnetic resonance (NMR) test utilizing $^{15}N_2$ as feeding gas indicated that NH_3 was produced by NRR rather than catalyst decomposition or contamination. In addition, the synergistic effect between NVs and doped ions contributes to enhancing NRR performance as well. Li *et al.* proposed that Fe-doped MoN_2 could act as a promising NRR catalyst through DFT calculations [123]. This is because that the NVs played a dominant role in adsorbing and activating nitrogen, while Fe-dopants mitigated the interaction between Mo-N_2 and promoted the second ammonia formation.

Based on the computational studies, transition metals (TMs) nitrides electrocatalysts have been confirmed to be more active towards NRR than HER. Therefore, we believe forming NVs in TMs nitrides as electrocatalysts can augment the number of active sites, which would in turn, enhance the NRR electrocatalytic performance. Additionally, isotopically labelled $^{15}N_2$ and $^{14}N_2$ are highly required to determine the detected ammonia origin, particularly for the NRR electrocatalysts which contain nitrogen species.

3.1.3. Sulfur vacancies

In the biological process, nitrogen fixation naturally occurs through nitrogenase enzymes, especially those containing a co-factor of iron-molybdenum-sulfur (FeMoS), which encourages the researchers to design catalysts based on the active components of nitrogenase enzymes to boost the NRR performance [126–129]. During the design of catalysts, the sulfur defects are indispensable parts in improving the NRR [126]. For example, defect-rich MoS_2 nanoflowers attained high FE of 8.34% and NH_3 yield of 29.28 μg h^{-1} mg^{-1} at −0.40 V *vs.* RHE, outperforming its defect-free counterparts. DFT calculations found that NRR on defected MoS_2 would proceed at a lower energy barrier of 0.60 eV in the distal associative pathway for the reaction of $^*NH \rightarrow {}^*NH_2$, relative to 0.68 eV in defect-free MoS_2. The positively charged plain Mo atoms at the edge of the defect could trigger the N_2 molecules, contributing to the decline of electrons between N atoms (Fig. 5a) [128–131].

The synergistic effect between sulfur vacancies (SVs) and doping of TMs brings about a new strategy for designing NRR catalysts. Suryanto *et al.* synthesized Ru nanoparticles on SVs-rich MoS_2 [129]. Ru/MoS_2 attained a high FE of 17.6% and an NH_3 yield

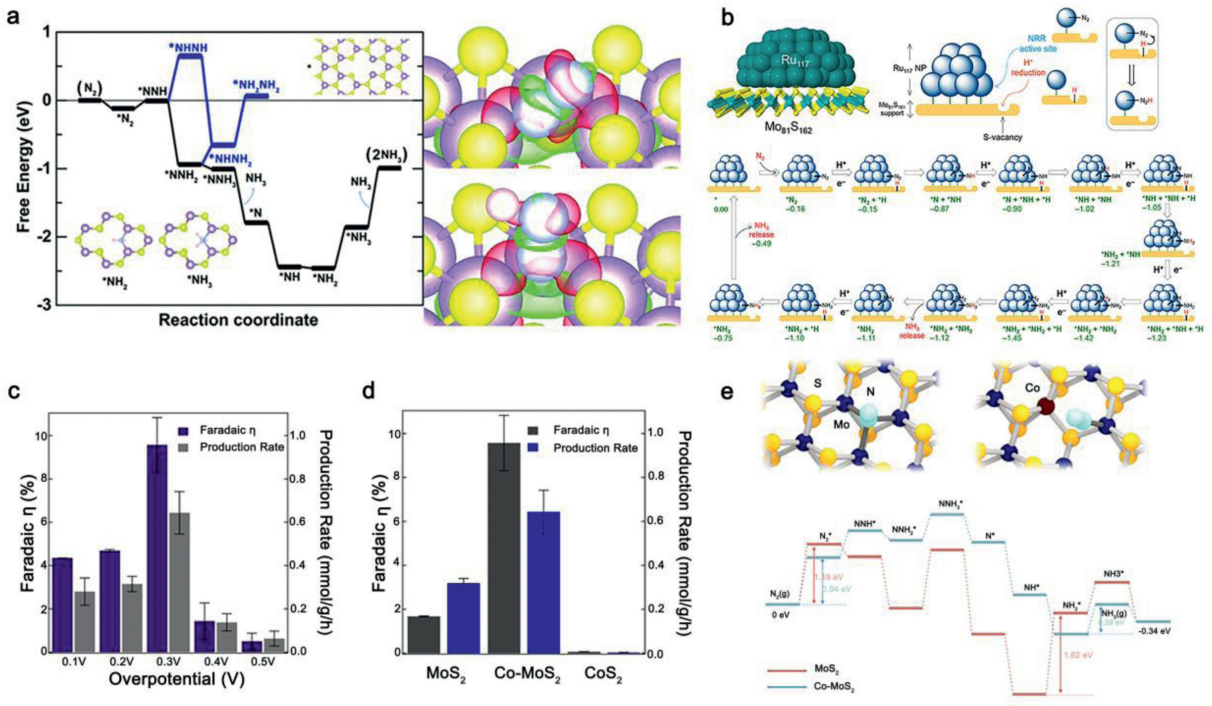

Fig. 5. (a) Free-energy profile for NRR at MoS_2 edge site. Reproduced with permission [126] (b) Scheme of Ru/2H-MoS_2 electronic properties and DFT for the mechanism of NRR. Reproduced with permission [129]. Copyright 2019, American Chemical Society. (c) Co-doped MoS_{2-x} NRR performance at different potentials. (d) NRR performance of MoS_{2-x}, Co-doped MoS_{2-x} and CoS_2 at −0.3 V. (e) Free-energy diagram of ammonia synthesis. Reproduced with permission [128]. Copyright 2019, American Chemical Society.

of 1.14×10^{-10} mol s^{-1} cm^{-2} at 50 °C. Both theoretical and experimental studies suggested that SVs in the MoS_2 matrix could act as the active H^+ binding sites and Ru nanoparticles as the active N_2 binding site (Fig. 5b). Recently, Zhang *et al.* synthesized a novel NRR electrocatalyst by doping Co into MoS_{2-x} nanosheets with rich SVs [128]. Co-doped MoS_{2-x} attained excellent performance, with an NH_3 yield of 0.63 mmol h^{-1} g^{-1} and FE of more than 10% at −0.3 V *vs.* RHE (Figs. 5c and d). From both experimental and theoretical perspectives, Co doping into defective MoS_{2-x} was eligible to efficiently induce NRR activity in its basal plane (Fig. 5e). DFT calculations indicated that in the first nitrogen adsorption step $N_2 \rightarrow {}^*N_2$ of NRR reaction, Co-doped MoS_{2-x} would proceed at a lower energy barrier of 0.94 eV than that of defective MoS_{2-x} (1.19 eV). The energy barrier for the rate-limiting step ${}^*NH \rightarrow {}^*NH_2$ was 1.62 eV in the undoped material, while reduced to 0.52 eV in the Co-doped case. Therefore, Co-doping led to a decrease in the overpotential required for electrolytic reaction, thus greatly improving the yield of ammonia and Faraday efficiency. The above endeavors not only show the NRR electrocatalyst with good activity under environmental conditions, but also pave the way for exploring TMs with SVs as NRR catalysts.

3.2. Dopants

Heteroatom doping can be advantageous to augmenting the active sites and reducing the energy barrier of NRR by building a unique electronic structure and coordination environment. It has also been thoroughly investigated as an effective way of improving the electrocatalytic activity of catalysts [132]. The latest advances in NRR electrocatalysts based on heteroatom doping will be recapitulated in this section.

3.2.1. Metal-atom doping

The heteroatom doping in carbon-based materials usually causes defects, which can not only tailor the electron structure of the neighboring carbon atoms for modulating polarity but also provide active sites to allow better adsorption of reactants. It has been established as supports for anchoring single metal atoms or double metal atoms in carbon-based materials to effectively tune the electronic properties of carbon. In this way, the performance of the materials will be boosted in all aspects, such as improved catalytic efficiency, increased utilization of atoms and lower cost [133,134].

Many research groups have constructed single atom catalysts (SACs) to reveal NRR efficiency through computational study. For example, Wei *et al.* performed spin-polarized DFT which proposed that the Fe-doped monolayer phosphorene (Fe@P) single metal atom catalyst (SMAC) could show superior catalytic efficiency than the bare matrix [135]. Interestingly, the doped Fe atom not only reduced the bandgap to 0.65 eV and sped up the charging-transfer process but also functioned as a catalytic active site for NRR, as clearly demonstrated by the spin-density and asymmetric charge distribution (Fig. 6a).

Choi *et al.* [136] have constructed a sequence of SACs on defective graphene comprising N defects and C vacancies towards NRR, and many of them (*e.g.*, $V@N_4$ and $Ti@N_4$) have served as effective catalysts with good selectivity and low overpotential. The calculation results indicated that H adsorption on SACs can be effectively suppressed by because the H adsorption energy on the SAC ($\Delta G(^*H)$) is greater than the H adsorption energy on the metal surface consisting of the corresponding metal atoms ($\Delta G_{surface}(^*H)$). For most metals, the values of $\Delta G_{SAC}(^*H) - \Delta G_{surface}(^*H)$ always remain in the positive region with a highly discrete trend (Fig. 6b). Similarly, Chen *et al.* prepared multiple single transition metal atoms (such as Ti, Pt and V) which were anchored on graphite carbon nitride (g-C_3N_4) containing NVs (TM@NVs-g-C_3N_4) [137]. Since the electrons in the TM orbits can be transferred to the $2p^*$ antibonding orbit of N_2, the hydrogenation efficiency of N_2 would be increased.

Apart from the SACs, Yang *et al.* investigated double-atom catalysts Fe-TM supported on graphene-based substrates (Fe-TMDA/GS) for electroreduction of nitrogen to ammonia [138]. The intro-

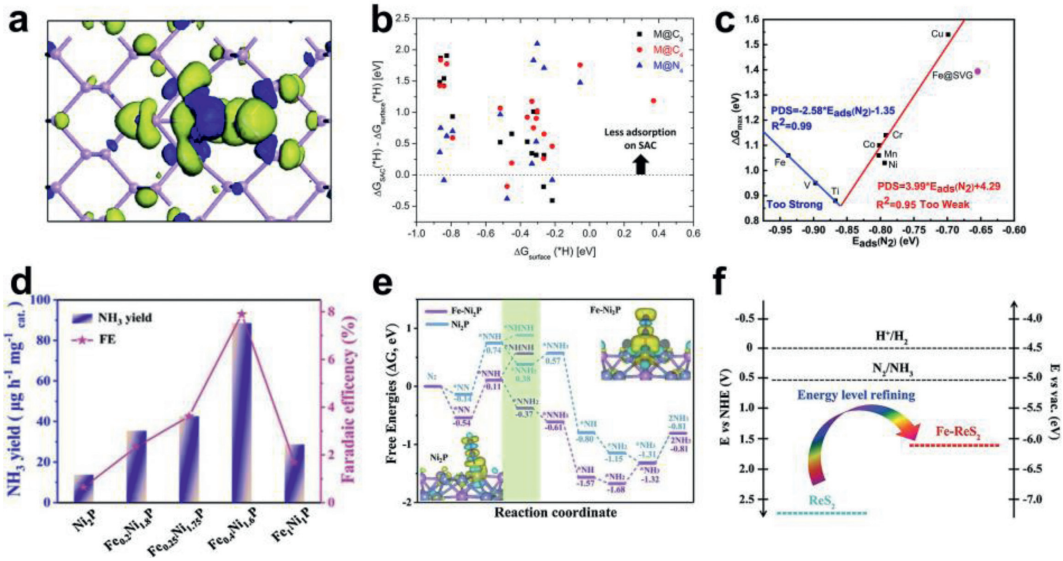

Fig. 6. (a) Top view of the distribution of spin density. The positive and negative densities of the spin are blue and yellow isosurfaces. Reproduced with permission [135]. Copyright 2018, Royal Society of Chemistry. (b) Differences between H adsorption free energy on the SAC ($\Delta G_{SAC}(*H)$) and adsorption free energy on the surface ($\Delta G_{surface}(*H)$) of the same metal atoms (eV). Horizontal dashed line denotes $\Delta G_{SAC}(*H) = \Delta G_{surface}(*H)$. Reproduced with permission [136]. Copyright 2018, American Chemical Society. (c) ΔG_{max} as a function of adsorption energy of N_2. Reproduced with permission [138]. Copyright 2019, Elsevier. (d) NH_3 yields and FEs of the pure Ni_2P catalyst as well as the Fe-doped Ni_2P catalysts with various Fe/Ni ratios (including $Fe_{0.2}Ni_{1.8}P$, $Fe_{0.25}Ni_{1.75}P$, $Fe_{0.4}Ni_{16}P$ and Fe_1Ni_1P). (e) The structures of intermediates for N_2 reduction on Fe-doped Ni_2P (001). The adsorption site is denoted by an asterisk (*) and the H, N, Ni, Fe and P atoms are shown in light pink, blue, gray-blue, brown and pink colors, respectively. Reproduced with permission [139]. Copyright 2020, Elsevier. (f) Band structure diagram for Fe-ReS_2 and pure ReS_2. Reproduced with permission [140]. Copyright 2020, John Wiley and Sons.

duction of a second metal atom facilitied the electron transfer between N_2 and graphene surface, thereby further enhancing the catalytic activity of NRR. As shown in Fig. 6c, the sequence of catalytic activity of Fe-TMDA/GS in NRR can be explained based on the inverted volcano diagram of ΔG_{max} and the adsorption energy N_2. According to the Sabatier principle, the catalytic activity of Fe TMDA/GS (TM = Cu) was obviously higher than that of single atom Fe catalyst, indicating that the regulation of TM improved the catalytic activity of NRR.

For practical concern, Guo *et al.* synthesized Fe-doped Ni_2P nanosheets by hydrothermal method as electrocatalyst for NRR [139]. Among the prepared Fe-doped Ni_2P nanosheets, $Fe_{0.4}Ni_{1.6}P$ exhibited superior NRR activity, with FE and ammonia yield of 7.92% and 88.51 μg h^{-1} $mg_{cat}{}^{-1}$, respectively, at −0.3 V *vs.* RHE than pure Ni_2P without Fe-doped (Fig. 6d). Theoretical calculations revealed the changes in the related intermediates in NRR and the energy barrier difference between Ni_2P (001) and Fe-doped Ni_2P (001), involving the transfer of six electrons and H^+ ions. The energy barrier of Fe-doped Ni_2P in the first potential determination step $*N–N* \rightarrow *NH–N*$ was 0.65 eV lower than that of Ni_2P, implying that Fe doping promoted N_2 activation and hydrogen selectivity in NRR. Due to the lower energy barrier, *NNH reacted in an associative distal pathway and thus was hydrogenated to form the reaction intermediate $*NNH_2$ instead of *NHNH (Fig. 6e). More recently, Lai *et al.* reported that low-valent metal doping to tune the energy level of electrocatalysts was effective in addressing the bottlenecks for HER and NRR [140]. They doped ReS_2 nanosheet with low-valent TMs (such as Fe, Co, Ni, Cu, and Zn) to form more active sites for N_2/H_2O chemisorption and electron transfer. Nitrogen-coated carbon nanofiber of Fe-doped ReS_2 nanosheets (Fe-ReS_2@N-CNF) obtained the highest electrochemical activity with NH_3 yield of 80.4 μg h^{-1} $mg_{cat}{}^{-1}$, which was 8-fold higher than bare ReS_2. Compared with the energy levels of undoped ReS_2 nanosheets, the energy levels of Fe-ReS_2 nanosheets were appropriately shifted to near the reduction potentials of H_2O and N_2 (Fig. 6f), simplifying the electron exchange process between the electrocatalysts and the reaction species [141]. DFT studies have shown that the introduction of low-valent transition metal into ReS_2 nanosheet structure could create abundant anchoring sites for direct adsorption and subsequent activation of N_2 molecules responsible for enhanced NRR performance.

3.2.2. Non-metal doping

Non-noble transition-metal-based catalysts have been studied in the production of lower-cost and high-efficient electrocatalysts for NRR. Due to facile synthesis, N-doping becomes the most popular in carbon-based electrocatalysts that are typically accomplished through the carbonization of N-rich substrates. As the nitrogen atom has a higher electronegativity than carbon atom, the electron cloud density of the neighboring carbon atom connected to nitrogen is lower, which is beneficial to the N_2 adsorption [142,143]. Moreover, the nitrogen atom has one more extranuclear electron and less electron affinity than carbon atom, yielding higher positive charge density of the carbon atom adjacent to the nitrogen. Furthermore, there exists conjugation interaction between the lone pair of electrons in the nitrogen atom and the π bond of the carbon atom; therefore, the N-doped carbons show excellent electrochemical performance. Yang *et al.* prepared N-containing hierarchical carbon foams (NCFs) by combining $ZnCl_2$ with cicada sloughs [144]. The NCFs attained a high NH_3 yield rate of 15.7 μg h^{-1} $mg_{cat}{}^{-1}$ and FE of 1.45% at −0.2 V *vs.* RHE. N-containing polymers or compounds can also be used as precursors in order to prepare N-doped carbon to promote NRR performance. Wang *et al.* introduced a technique for developing a nitrogen-doped carbon membrane (NCM) with a hierarchical structure for NRR [145]. The pristine NCMs obtained an NH_3 yield of 0.08 g m^{-2} h^{-1} at −0.3 V *vs.* RHE and FE of 5.2% at −0.2 V *vs.* RHE. By using semiconductive NCMs with high porosity as a loading substrate for Au nanoparticles, the efficiency improved to 0.361 g m^{-2} h^{-1} and 22%, respectively.

Inspired by the improved electrocatalytic performance generated by the N-doping materials, some groups have constructed the synergistic doping species models into the carbon matrix. The incorporation of nonmetals such as boron into the carbon matrix can

redistribute electron density, where the electron-deficient boron sites offer superior binding capabilities to the N_2 molecules [146]. Yu *et al.* synthesized boron atoms incorporated into graphene sheets (BC_3) by thermal reduction of graphene oxide [146]. BC_3 attained ammonia yield rate and FE of 9.8 μg h^{-1} cm^{-2} and 10.8%, respectively, at −0.5 V *vs.* RHE. The NH_3 yield and FE results were 5 times and 10 times fold higher than the undoped graphene, respectively. In fact, the pristine boron nitride (BN) replaced the C atom at the edge or defect sites of the G framework caused by the sluggish ammonia desorption. To overcome this effect, Mao *et al.* developed a single B-atom incorporated on BN edge (B@BN) with an incredibly low overpotential of only 0.13 V using a distal pathway. In addition, with a low energy barrier of 0.35 eV, the created NH_3 could be quickly removed [147].

Besides being a single non-metal element for doping, Bi-nonmetal can be developed as an NRR catalyst because the more flexible configurations could activate the adjacent carbon atoms and put them into carbon-based matrixes. Tian *et al.* studied N/S co-doped graphene (NSG) as an effective metal-free catalyst for NRR [148]. The as-prepared NSG performed an NH_3 yield of 7.7 μg h^{-1} mg_{cat}^{-1} and FE of 5.8% at −0.6 V *vs.* RHE higher than undoped and single-doped counterparts. The existence of pyrrole-N, pyridine-N, and thiophene-S was expected to trigger positively charged on adjacent C atoms, which could facilitate N_2 adsorption, weaken N≡N bond, and boost electron transfer.

3.3. Amorphisms

Amorphous materials possessing dangling bonds raise the number of unsaturated coordination sites as well as increase the number of catalytic defects, thereby improving their catalytic activity and promoting NRR efficiency. Amorphous catalysts have been thoroughly researched for their high performance in different electrocatalytic reactions (such as oxygen evolution reaction, HER and NRR) and most of them have shown better performances over their crystalline forms [149–152]. Throughout this section, we will outline the recent progress of the amorphous materials (noble and non-noble metals) in the NRR.

3.3.1. Amorphous noble metal-based materials

Noble metals are applied broadly as electrocatalysts for a variety of reactions as they can provide strong binding for a wide range of reactants and have good electric conductivity. Lately, noble metal-based catalysts, including Au [153–155], Rh [156], Pt [157] and Ru [158] have been widely utilized as NRR electrocatalysts.

Through crystallinity modulation, precious metal-based materials can be transferred to amorphous materials to further create defects offering active sites. Li *et al.* [153] transformed crystallized Au nanoparticles (~5 nm) to the amorphous state and used reduced graphite oxide (rGO) as a platform for anchoring Au nanoparticles (*a*-Au/CeO_x-rGO) by an easy co-reduction process under ambient conditions. Low-crystalline cerium oxides (CeO_x) played a critical role in enhancing NRR performance because they had a high number of unsaturated coordination sites. As a consequence, *a*-Au/CeO_x-rGO with low Au loading of 1.31 wt% achieved an ammonia yield of 8.3 μg h^{-1} mg^{-1} and FE of 10.10% at −0.2 V *vs.* RHE at ambient temperature, better than its bare equivalent without CeO_x (*c*-Au/rGO, with an NH_3 rate of 3.5 μg h^{-1} mg^{-1} and FE of 3.67%) (Figs. 7a–c). Moreover, there was no hydrazine formed in this work, proving that the catalyst was effective in boosting both the activity and the selectivity.

As HER occupies a dominant position on the noble metal catalysts, the NRR activity cannot be fully substantiated. Generally, the expensiveness and paucity of noble metals are considered as obstacles for practical large-scale applications. To address these thorny issues, alloying the noble metals and TMs is proposed as a solution to generate various active sites and enhance the catalytic performance. As shown by Shi *et al.*, the ultrafine Pd_xCu_{1-x} amorphous nanoclusters anchored on rGO ($Pd_{0.2}Cu_{0.8}$/rGO) were prepared using a co-reduction method [159]. The X-ray diffraction (XRD) pattern of $Pd_{0.2}Cu_{0.8}$/rGO has no obvious bimetallic peaks compare with Pd/rGO and Cu/rGO except for the diffraction peaks of reduced graphene oxide, which indicates its amorphous state (Fig. 7d). By tuning the bimetallic ratio of Cu and Pd, the optimal performance was attained for $Pd_{0.2}Cu_{0.8}$/rGO composite with an NH_3 yield of 2.80 μg h^{-1} mg^{-1} at −0.2 V *vs.* RHE (Fig. 7e). As the electronic interaction for both Cu and Pd considerably altered the electronic states of the monometal compounds, the NH_3 yield provided by the bimetallic $Pd_{0.2}Cu_{0.8}$/rGO was 2.1 times higher than that of the Pd/rGO and 2.4 times higher than that of the Cu/rGO equivalents (Fig. 7f). The outstanding catalytic performance of alloy catalysts with low noble metal proportions would highly inspire the researchers to deepen study about amorphous bimetallic or even trimetallic catalysts on NRR process in the future.

3.3.2. Amorphous non-noble metal-based materials

Lately, non-noble metals (particularly TMs) have emerged as potential candidate electrocatalysts for NRR owing to their abundant resources, low cost, and favorable catalytic activity [160]. Considering the fact that works in this field are few, researchers should devote more effort to unraveling the effect of different amorphous non-noble metals on catalytic efficiency of NRR. As we have already concluded, existing OVs in TMOs could play an active role in the adsorption of reactants as well as reaction intermediates, thus decreasing the energy activation barrier and boosting electrocatalytic efficiency. Lv *et al.* prepared $Bi_4V_2O_{11}/CeO_2$ composite with amorphous phase (BVC-A) consisting of abundant OVs, which gave superior electrocatalytic NRR efficiency with an ammonia production of 23.21 μg h^{-1} mg^{-1} and FE of 10.16% at −0.2 V *vs.* RHE under ambient conditions (Fig. 7g) [112]. It was also demonstrated that the mole ratios of Ce/Bi were crucial for forming the amorphous $Bi_4V_2O_{11}$ which possessed rich defects, as illustrated by XPS and high resolution transmission electron microscope (HRTEM) results (Fig. 7h). The disturbed structure was abundant with dangling bonds, which provided a high concentration of defect sites and decreased the energy barrier, serving as a good catalyst for enhancing NRR activity.

In addition to BVC-A, a sequence of amorphous Sn/crystalline SnS_2 (Sn/SnS_2) nanosheets were synthesized by Li *et al.* through the hydrothermal method, followed by *in situ* electrochemical reduction [161]. The different percentages of amorphous Sn could be tuned through selecting electrolytes with various pH values. In N_2-saturated 0.1 mol/L phosphate buffer solution (PBS), Sn/SnS_2 electrocatalyst attained a high ammonia yield of 23.8 μg h^{-1} mg^{-1} at −0.8 V *vs.* RHE and FE of 6.5% at −0.7 V *vs.* RHE. No observable hydrazine was produced, implying its favorable selectivity for NH_3. Moreover, NMR proved that the cathode reduction products were derived from the reduced N_2. These findings will provide guidance for us to investigate other NRR catalysts based on TMs *via* using the amorphous approach in the future.

3.4. Edges/corners

The surface area plays a key role in various reactions, as the reactants are adsorbed and bound to the catalyst surface. The electrical fields can be concentrated by the high-curvature structure which will influence ion concentrations [162]. Therefore, creation of edges or corners may be an efficient way to improve the performance of NRR. Song *et al.* [163] have created a specific carbon nanospikes (CNS) with scratchy surfaces made up of sharp spikes.

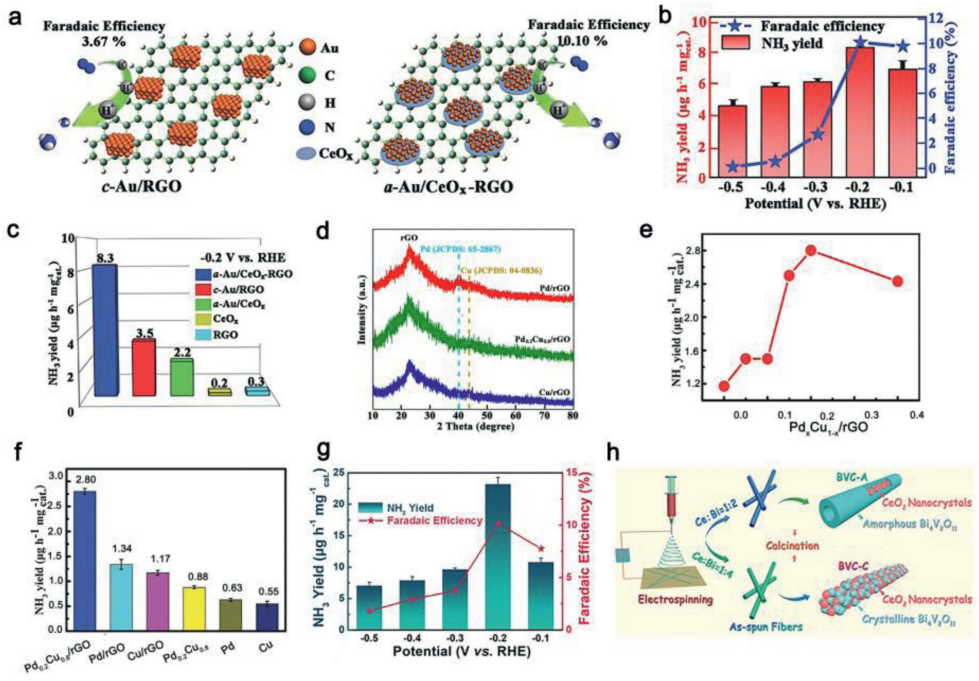

Fig. 7. (a) Schematic representation for the electrochemical NRR by catalysts of *c*-Au/rGO and *a*-Au/CeO_x-rGO. (b, c) NRR performance of *a*-Au/CeO_x-rGO and other catalysts at −0.2 V *vs.* RHE, Reproduced with permission [153]. Copyright 2017, John Wiley and Sons. (d) Representative XRD patterns of Cu/rGO, Pd/rGO and $Pd_{0.2}Cu_{0.8}$/rGO. (e, f) NRR performance of $Pd_{0.2}Cu_{0.8}$/rGO and different catalysts at −0.2 V *vs.* RHE. Reproduced with permission [159]. Copyright 2018, John Wiley and Sons. (g) NRR performance of BVC-A at −0.2 V *vs.* RHE. (h) Illustration of fabricating BVC-A and BVC-crystalline (BVC-C) NRR electrocatalysts. Reproduced with permission [112]. Copyright 2018, John Wiley and Sons.

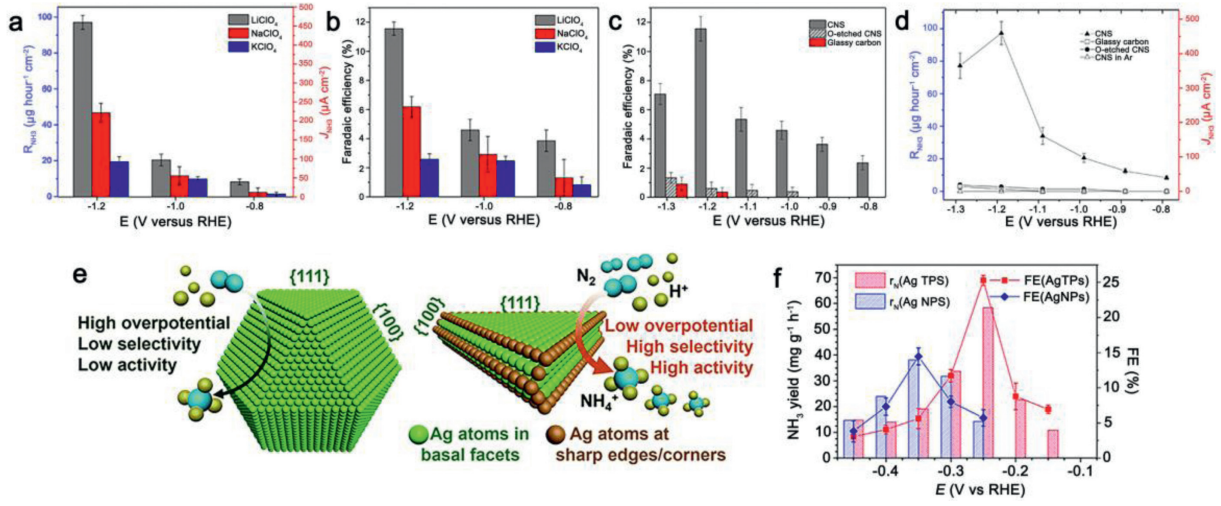

Fig. 8. (a, b) Ammonia output and FE of CNS in different countercations with the order of $Li^+ > Na^+ > K^+$. (c, d) FEs and ammonia formation rates of various catalysts. Reproduced with permission [163]. Copyright 2018, American Association for the Advancement of Science. (e) Schematic diagram of NRR on triangular AgTPs and rounded AgNPs. (f) NRR performance of AgTPs and AgNPs. Reproduced with permission [164]. Copyright 2019, The Royal Society of Chemistry.

The nitrogen-doped CNS contained multiple-oriented spikes of approximately 50–80 nm in length, ending at approximately ~1 nm in the tip, serving as a good physical catalyst to stimulate the electrical field. The pure CNS demonstrated higher NRR efficiency with an outstanding NH_3 yield of 97.18 μg h^{-1} cm^{-2} and a good FE of 11.5% at −1.19 V *vs.* RHE than oxygen-plasma etched (O-Etched) CNS without a sharp tip.

The electrolyte cations with the sequence of $Li^+ > Na^+ > K^+$ have been determined to be critical during NRR process, implying that the counterions with the smallest ionic radius could enhance the electric field and serve as promoters to enhance the N_2 concentration close to the tips (Figs. 8a and b), in addition to creating a dehydrated cation shield around the tip to block the water and the proton to pass through. After Ar plasma treatment, the efficiency of NRR became very low, showing the beneficial impact of the spike structure (Figs. 8c and d). These outcomes showed that the NRR was driven by the powerful electric fields from the catalyst spike.

More recently, Gao *et al.* reported that NRR efficiency could be improved by using Ag triangular nanoplates (AgTPs) with sharp edges as catalysts [164]. The rounded Ag nanoparticles (AgNPs) were mainly wrapped by {111} and {100} facets, which served as active sites for H^+/e^- transfer and nitrogen fixation. While for AgTPs, a large number of atoms were located at the sharp edges and corners with lower coordination numbers and stronger ability to adsorb nitrogen species (Fig. 8e). Therefore, the energy barrier of the reaction determination step *NN → *NNH was highly reduced, promising a good yield and high efficiency at a lower applied po-

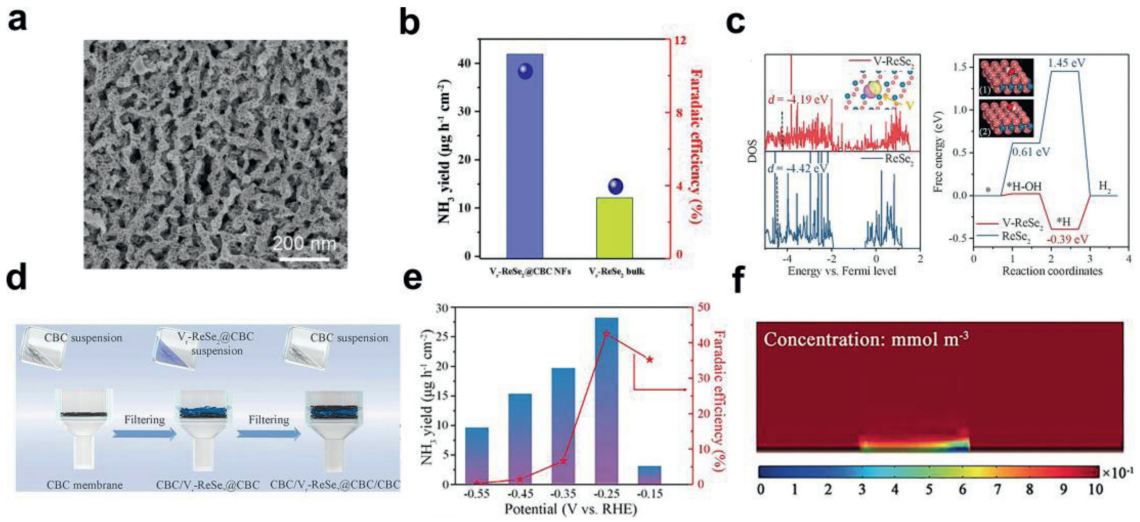

Fig. 9. (a) SEM image of Pd_3Cu_1 alloy. Reproduced with permission [168]. Copyright 2019, Elsevier. (b) NH_3 yield (bar graph) and Faradaic efficiency (blue point) by using Vr-$ReSe_2$@CBC NFs and Vr-$ReSe_2$ bulk as contrast samples. (c) DOS for V-$ReSe_2$ and $ReSe_2$ models, as well as the charge density difference of V-$ReSe_2$ (The pink and yellow areas present electrons accumulation and depletion, respectively) (left figure), and free energy diagrams for nitrogen reduction reaction on the surface of V-$ReSe_2$ and $ReSe_2$ catalysts (right figure). (d) Schematic diagram of synthesis process of CBC@Vr-$ReSe_2$@CBC. (e) NRR performance (NH_3 yield and Faradaic efficiency) of CBC@Vr-$ReSe_2$@CBC NFs in 0.1 mol/L Na_2SO_4 electrolyte under ambient conditions. (f) Distributions of concentration of H^+ ions in the electrode in the COMSOL multiphysics simulations. Reproduced with permission [169]. Copyright 2020, John Wiley and Sons.

tential for NRR. AgTPs with sharp edges have attained an ammonia yield of 58.5 mg g_{Ag}^{-1} h^{-1} and a high FE of 25% at an overpotential of −0.25 V *vs.* RHE under environmental conditions. In contrast, by using rounded Ag nanoparticles, the FE and NH_3 yield have been decreased significantly to 16% and 38 mg g_{Ag}^{-1} h^{-1} respectively at a larger overpotential −0.35 V *vs.* RHE (Fig. 8f). Such enhanced performance verified that the AgTPs was one of the most efficient transition metal catalysts for NRR.

3.5. Porousness

Porousness existed in the structures usually possess rich channels, which could facilitate the N_2 enrichment, prolong N_2 residue time, slow down the escape of reaction intermediates, shorten the transport path of electrons and protons, and further accelerate NRR process. For example, Ying *et al.* transformed commercial Fe_3O_4 into porous structure based on deep eutectic solvent regeneration strategy [165]. The flaky and porous structure endowed the treated Fe_3O_4 with large active surface area and high porosity. Compared with commercial Fe_3O_4, the treated material showed better electrocatalytic performance, with a high yield of 12.09 μg h^{-1} mg_{cat}^{-1} and a FE of 34.38% at 0.1 mol/L Na_2SO_4. Besides, alloying two metals can change the electronic structure of each metal, and then synergistically change the adsorption energy of reactants on the catalyst [166]. For example, Yu *et al.* proposed a one-pot reduction method for direct synthesis of bimetallic Ag_3Cu porous network (Ag_3Cu BPNs) [167]. Due to the porous network and bimetallic composition, Ag_3Cu BPNs exhibited a high ammonia yield of 24.59 μg h^{-1} mg_{cat}^{-1} and a superior FE of 13.28% in 0.1 mol/L $NaSO_4$. Similarly, Pang *et al.* designed a 3D layered interconnected porous network Pd/Au alloy with excellent NRR performance (Fig. 9a) [168]. The large specific surface area and high active site density effectively inhibited HER and contributed to an ammonia yield up to 39.9 μg h^{-1} mg_{cat}^{-1}. In terms of stability, the alloy maintained 100% of the original activity after 18 h of operation.

However, the enhanced N_2 activation due to porous active site modifications such as vacancy formation and doping, inevitably leads to a reduction in the proton coupling potential and thus enhances the occurrence of the competitive hydrogen precipitation reaction. The trap engineering strategies discussed in the previous sections do not effectively address this issue. Porous materials provide an alternative solution, as they may involve processes such as interfacial wettability and pore-induced diffusion that can facilitate enhanced nitrogen fixation while reducing the hydrogen precipitation performance of the catalyst. Recently, some progress has been made in enhancing electrocatalytic nitrogen fixation through modification of interfacial wettability. Lai *et al.* prepared vacancy-rich $ReSe_2$@carbonized bacterial cellulose nanofibers (Vr-$ReSe_2$@CBC NFs) by heat treatment methods [169]. Monolayer porous CBC as a porous carrier enabled uniform distribution of Vr-$ReSe_2$ nanosheets compared to unloaded selenium-rich vacant $ReSe_2$, thus enhancing their charge transfer capacity and producing higher ammonia yields (Fig. 9b). The total density of states (DOS) plots and free energy compared to $ReSe_2$ bulk are shown in Fig. 9c, with d-band centering at 4.19 eV and 4.42 eV for V-$ReSe_2$ and $ReSe_2$, respectively. This indicated that more electrons were distributed around the Fermi energy level, causing stronger interaction between N_2/water and the V-$ReSe_2$ surface, and allowing the electrons to be easily transferred to N_2/water. In such way, the adsorption and activation of V-$ReSe_2$ to both N_2 and water were enhanced. To confine HER, the same group buried Vr-$ReSe_2$@CBC nanofibers between two CBC layers (CBC/Vr-$ReSe_2$@CBC/CBC) (Fig. 9d). The CBC layers can achieve a hydrophobic interior of Vr-$ReSe_2$@CBC using trace evaporated water, which hindered the HER process and reduced the FE. Therefore, a large amount of moist N_2 gas was injected into the Vr-$ReSe_2$@CBC NFs and aggregated on its surface under thermodynamically favorable adsorption to facilitate the NRR process. In terms of electrochemical properties, the CBC/Vr-$ReSe_2$@CBC/CBC exhibited a FE four times higher than that of Vr-$ReSe_2$@CBC (Fig. 9e). The H^+ concentration near the Vr-$ReSe_2$@CBC interface was significantly reduced using COMSOL multiphysics simulations (Fig. 9f), indicating that the CBC layer covering the top of Vr-$ReSe_2$@CBC was hydrophobic and porous to water molecules.

Generally, defect engineering, including generating cations/anions vacancies, doping defects, creating amorphous structures, edge defects, and porous defects has been demonstrated to be effective in enhancing both activity and selectivity of the NRR (summarized in Table 1) [26,84,94,112–115,117–120,125–128,139,140,146,155,159,161,163,164,167,170–195].

Table 1
A brief summary of typical NRR electrocatalysts with defects identified in the latest years and their catalytic efficiency.

Catalyst	Electrolyte	Ammonia yield	Faradaic efficiency (%)	Potential (V, *vs.* RHE)[a]	Defect type	Ref.
MnO_x NA/TM	0.1 mol/L Na_2SO_4	1.63×10^{-10} mol s^{-1} cm^{-2}	11.40	−0.5	Vacancy	[84]
r-CeO_2	0.1 mol/L Na_2SO_4	16.4 μg h^{-1} mg_{cat}^{-1} (−0.5 V)	3.7 (−0.4 V)		Vacancy	[170]
MoS_2	0.1 mol/L Na_2SO_4	46.1×10^{-11} mol s^{-1} cm^{-2}	4.58	−0.5	Vacancy	[171]
Zn-Co_3O_4	0.1 mol/L HCl	22.71 μg h^{-1} mg_{cat}^{-1}	11.9	−0.3	Vacancy	[172]
MoO_2	0.1 mol/L HCl	12.20 μg h^{-1} mg_{cat}^{-1}	8.2	−0.15	Vacancy	[173]
d-TiO_2/TM	0.1 mol/L HCl	1.24×10^{-10} mol s^{-1} cm^{-2}	9.17	−0.15	Vacancy	[174]
LaxFe$O_{3-\delta}$	0.1 mol/L Li_2SO_4	22.1 μg h^{-1} mg_{cat}^{-1} (−0.5 V)	25.6 (−0.3 V)		Vacancy	[175]
WO_3	0.1 mol/L HCl	4.2 μg h^{-1} mg_{cat}^{-1}	6.8	−0.12	Vacancy	[176]
ZrO_2	0.1 mol/L Na_2SO_4	9.63 μg h^{-1} mg_{cat}^{-1}	12.1	−0.7	Vacancy	[177]
TiO_2–800	0.1 mol/L HCl	3.0 μg h^{-1} mg_{cat}^{-1}	6.5	−0.12	Vacancy	[120]
MV-MoN@NC	0.1 mol/L HCl	76.9 μg h^{-1} mg_{cat}^{-1}	6.9	−0.2	Vacancy	[178]
Ta_2O_5	0.1 mol/L HCl	15.9 μg h^{-1} mg_{cat}^{-1}	8.9	−0.7	Vacancy	[113]
Ru/TiO_2-OVs	0.1 mol/L HCl	2.11 μg h^{-1} cm^{-2} (−0.15 V)	0.72 (−0.1 V)		Vacancy	[119]
α-Fe_2O_3	0.1 mol/L KOH	32.13 μg h^{-1} mg_{cat}^{-1}	6.63	−0.3	Vacancy	[118]
TiO_2/$Ti_3C_2T_X$	0.1 mol/L HCl	32.17 μg h^{-1} mg_{cat}^{-1} (−0.55 V)	16.07 (−0.45 V)		Vacancy	[114]
OV-2D TiO_2	0.1 mol/L H_2SO_4	35.6 μg h^{-1} mg_{cat}^{-1} (−0.8 V)	5.3 (−0.7 V)		Vacancy	[117]
NC-Cu single atom	0.1 mol/L KOH	53.3 μg h^{-1} mg_{cat}^{-1}	13.8	−0.35	Dopant	[179]
N-doped CNS	0.25 mol/L $LiClO_4$	97.18 ± 7.13 μg h^{-1} cm^{-2}	11.56±0.85	−1.19	Dopant	[163]
Fe/TiO_2	0.1 mol/L Na_2SO_4	43.14 μg h^{-1} mg_{cat}^{-1}	16.3	−0.3	Dopant	[180]
Fe-doped Ni_2P	0.1 mol/L HCl	88.51 μg h^{-1} mg_{cat}^{-1}	7.92	−0.3	Dopant	[139]
Au-Fe_3O_4	0.1 mol/L KOH	21.42 μg h^{-1} mg_{cat}^{-1}	10.54	−0.2	Dopant	[115]
NV-W_2N_3	0.1 mol/L KOH	3.8×10^{-11} mol s^{-1} cm^{-2}	11.67	−0.2	Dopant	[125]
BNC-NSs	0.05 mol/L H_2SO_4	15.7 μg h^{-1} mg_{cat}^{-1}	8.1	−0.4	Dopant	[181]
Cu-doped TiO_2	0.5 mol/L $LiClO_4$	21.31 μg h^{-1} mg_{cat}^{-1}	21.99	−0.55	Dopant	[182]
P-doped graphene-CP	0.5 mol/L $LiClO_4$	32.33 μg h^{-1} mg_{cat}^{-1}	20.82	−0.65	Dopant	[183]
B-doped graphene	0.05 mol/L H_2SO_4	9.8 μg h^{-1} cm^{-2}	10.8	−0.5	Dopant	[146]
Ru-Mo_2CT_X MXene	0.5 mol/L K_2SO_4	40.57 μg h^{-1} mg_{cat}^{-1}	25.77	−0.3	Dopant	[184]
Mo-MnO_2 NFs	0.1 mol/L Na_2SO_4	36.6 μg h^{-1} mg^{-1} (−0.5 V)	12.1 (−0.4 V)		Dopant	[185]
Au/TiO_2	0.1 mol/L HCl	21.4 μg h^{-1} mg_{cat}^{-1}	8.11	−0.2	Dopant	[155]
F-doped MoS_2	0.05 mol/L H_2SO_4	35.7 μg h^{-1} mg_{cat}^{-1}	20.6	−0.2	Dopant	[186]
Fe-ReS_2@N-CNF	0.1 mol/L Na_2SO_4	80.4 μg h^{-1} mg_{cat}^{-1}	12.3	−0.2	Dopant	[140]
Au/TiO_2	0.01 mol/L HCl	64.6 μg h^{-1} mg_{cat}^{-1}	29.5	−0.4	Dopant	[187]
Au/C_3N_4	5 mmol/L H_2SO_4	1.3 mg h^{-1} mg_{Au}^{-1}	11.1	−0.1	Dopant	[188]
Sn/SnS_2	0.1 mol/L PBS	23.8 μg h^{-1} mg_{cat}^{-1} (−0.8 V)	6.5 (−0.7 V)		Amorphism	[161]
$Pd_{0.2}Cu_{0.8}$/rGO	0.1 mol/L KOH	2.8 μg h^{-1} mg_{cat}^{-1}	< 1	−0.2	Amorphism	[159]
Sn/SnS_2	0.1 mol/L PBS	23.8 μg h^{-1} mg_{cat}^{-1} (−0.8 V)	6.5 (−0.7 V)		Amorphism	[161]
$Bi_4V_2O_{11}$/CeO_2	0.1 mol/L HCl	23.21 μg h^{-1} mg_{cat}^{-1}	10.16	−0.2	Amorphism	[112]
$Ni_{0.50}Fe_{0.50}B$	0.1 mol/L KOH	3.24 μg h^{-1} cm^{-2}	3.19	−0.3	Amorphism	[94]
MoS_3	0.5 mol/L $LiClO_4$	51.7 μg h^{-1} mg^{-1}	12.8	−0.3	Amorphism	[189]
H-CrO_x/C-550	0.1 mol/L Na_2SO_4	19.10 μg h^{-1} mg_{cat}^{-1}	1.4	−0.7	Amorphism	[190]
MoS_2 nanodots/reduced graphene oxide	0.1 mol/L Na_2SO_4	16.41 μg h^{-1} mg_{cat}^{-1} (−0.75 V)	27.93 (−0.35 V)		Edge/corner	[191]
MoS_2	0.1 mol/L Li_2SO_4	43.4 μg h^{-1} mg_{cat}^{-1}	9.81	−0.2	Edge/corner	[192]
AgTPs	0.1 mol/L K_2SO_4	58.5 mg g_{Ag}^{-1} h^{-1}	25	−0.25	Edge/corner	[164]
MoS_2	0.1 mol/L Na_2SO_4	8.08×10^{-11} mol s^{-1} cm^{-2}	1.17	−0.5	Edge/corner	[127]
Co-MoS_2	0.1 mol/L H_2SO_4	0.63 mmol h^{-1} g^{-1}	10	−0.3 (*vs.* NHE[b])	Edge/corner	[128]
MoS_2 nanoflowers	0.1 mol/L Na_2SO_4	29.28 μg h^{-1} mg_{cat}^{-1}	8.34	−0.4	Edge/corner	[126]
Mo_2C/C	0.5 mol/L Li_2SO_4	34.0 μg hs^{-1} mg_{cat}^{-1}	7.8	−0.3	Porousness	[193]
Porous β-FeOOH	0.05 mol/L H_2SO_4	2860 μg_{NH3} mg_{Au}^{-1} h^{-1}	14.2	−0.4	Porousness	[194]
Ag_3Cu BPNs	0.1 mol/L Na_2SO_4	24.59 μg h^{-1} mg_{cat}^{-1}	13.28	−0.5	Porousness	[167]
AuCuB	0.1 mol/L Na_2SO_4	13.2 μg h^{-1} mg_{cat}^{-1}	12.87	−0.5	Porousness	[195]
pAu/NF	0.1 mol/L Na_2SO_4	9.42 μg h^{-1} cm^{-2}	13.36	−0.2	Porousness	[26]

[a] RHE: reversible hydrogen electrode.
[b] NHE: normal hydrogen electrode.

4. Summary and challenges

In this review, recent research progress on the effect of several different defect structures in defect engineering technologies on electrochemical NRR is comprehensively investigated. For vacancy (*e.g.*, OVs, SVs and NVs) defect structures, the alteration of the local electrons allows the vacancy to act as the active center of NRR, which can effectively adsorb and activate N_2 molecules. DFT theoretical calculations show that the presence of vacancies largely reduces the energy barrier required for the N_2 hydrogenation reaction compared to catalysts without vacancy structures. For doped defect structures, theoretical calculations are discussed to summarize the feasibility of atom doping of different metal species as active sites to tune the electron configuration and thus improve the nitrogen fixation capacity. Meanwhile, non-metals are also an important means of doping, such as nitrogen doping, where the smaller affinity of nitrogen progeny and the existence of conjugation between its lone pair of electrons and π-bonds of carbon atoms promise the excellent properties. Compared to crystalline structures, amorphous catalysts can help expose more defective structures with active sites, and both volume- and surface-constrained electrocatalytic processes may exist in amorphous catalysts, thus ensuring a larger electrolyte-catalyst interface. The presence of edge defect structures enriches the dangling bonds on the catalyst surface, which provides a high concentration of defect sites, lowers the energy barrier and serves as a good catalyst for enhanced NRR activity. Some recent studies have shown that the selectivity of ammonia and hydrogen corresponding to different kinds of exposed high-energy atoms on the edge differs, so subsequent studies on the cross section may involve the separation of active sites to achieve simultaneous enhancement of selectivity and activity for ammonia. Porousness as another popular defective structure has abundant specific surface area and provides a large number of active site structures, which facilitates catalyst conduc-

tivity enhancement and nitrogen activation. Hydrogen evolution reaction occurs on proton-rich hydrophilic surfaces, and modification of interfacial properties by porous hydrophobic materials can selectively attenuate proton coupling and thus enhance the selectivity for ammonia. Besides, the types of defects are often not present in a single structural form; for example, there may be simultaneous abundant edges/corners around the porous structures. Amorphous and doped structures may be accompanied by the formation of vacancies (*e.g.*, OVs and SVs). These defect types interact and interconnect with each other while exposing abundant active sites, which play an indispensable role in improving NRR performance. Despite of some pioneering and creative research on defect engineering of electrocatalytic materials, this area of research is still in its preliminary stage and there are substantial challenges ahead that need to be properly addressed.

(1) The controlled generation of defects. The current methods of preparing defects either *in situ* or post-processing are not effective in achieving a single presence of defects, which impedes the study of their mechanism during electrocatalytic reactions and the understanding of the important role they play. This calls for precise synthetic methods to control the generation of defects, which will help to isolate the complex factors in the electrochemical process and pave the way for a comprehensive and profound understanding of defect effects.
(2) Large-scale synthesis of defective electrocatalysts. From the perspective of materials synthesis, the key properties such as morphology, electronic and energy band structure, and charge transfer capability of defective catalytic materials can be optimally designed by controlled synthetic pathways to achieve efficient nitrogen fixation. However, since defect formation in catalysts is a high-energy process and is currently prepared only in the laboratory, the cost issue of defect fabrication deserves researchers' attention. Therefore, an effective strategy for large-scale synthesis of defective electrocatalysts is urgently needed to meet the economic demand for practical applications in electrocatalytic nitrogen fixation.
(3) Defect characterization. In general, conversion and reorganization of active sites may occur during reduction reactions, and traditional *in situ* characterization methods have difficulty in reproducing such structural changes. Therefore, *in situ*/operational measurements with high spatial, spectral and temporal resolution have become an effective technique for gaining insight into the role of defects in electrocatalytic reactions. This study responds to a real catalytic mechanism that can guide researchers to effectively design and protect the active sites of catalysts and extend the catalyst lifetime.

In summary, the progress of defect engineering for guiding the design of NRR electrocatalysts were discussed. Although future research work in this area will be more challenging, we believe that the combination of accurate characterization techniques, controlled synthetic methods and scientifically rigorous studies, together with reasonable model simulations, will further accelerate the development of defect structure systems driven NRR electrocatalysts. We are convinced that the field of electrocatalytic nitrogen fixation will eventually achieve greater breakthroughs.

Declaration of competing interest

The authors declare that they have no known competing financial interests or personal relationships that could have appeared to influence the work reported in this paper.

Acknowledgment

This work was supported by the National Natural Science Foundation of China (Nos. 22075133 and 21701086).

References

[1] B.H.R. Suryanto, K. Matuszek, J. Choi, et al., Science 372 (2021) 1187–1191.
[2] K. Li, S.Z. Andersen, M.J. Statt, et al., Science 374 (2021) 1593–1597.
[3] X. Kong, H.Q. Peng, S. Bu, et al., J. Mater. Chem. A 8 (2020) 7457–7473.
[4] X. Zhao, G. Hu, G.F. Chen, et al., Adv. Mater. 33 (2021) 2007650.
[5] M. Wang, M.A. Khan, I. Mohsin, et al., Energy Environ. Sci. 14 (2021) 2535–2548.
[6] Y. Wan, H. Zhou, M. Zheng, et al., Adv. Funct. Mater. 31 (2021) 2100300.
[7] Y. Tan, L. Yan, C. Huang, et al., Small 17 (2021) 2100372.
[8] K.A. Brown, D.F. Harris, M.B. Wilker, et al., Science 352 (2016) 448.
[9] S. Shang, W. Xiong, C. Yang, et al., ACS Nano 15 (2021) 9670–9678.
[10] L. Li, C. Tang, X. Cui, et al., Angew. Chem. Int. Ed. 60 (2021) 14131–14137.
[11] Y. Feng, Z. Zhang, K. Zhao, et al., J. Colloid Interface Sci. 583 (2021) 499–509.
[12] F. Gorky, J.M. Lucero, J.M. Crawford, et al., ACS Appl. Mater. Interfaces 13 (2021) 21338–21348.
[13] A. Anastasopoulou, R. Keijzer, S. Butala, et al., J. Phys. D: Appl. Phys. 53 (2020) 234001.
[14] K. Han, J. Luo, Y. Feng, et al., Energy Environ. Sci. 13 (2020) 2450–2458.
[15] C.J.M. van der Ham, M.T.M. Koper, D.G.H. Hetterscheid, Chem. Soc. Rev. 43 (2014) 5183–5191.
[16] X. Cui, C. Tang, Q. Zhang, Adv. Energy Mater. 8 (2018) 1800369.
[17] G. Qing, R. Ghazfar, S.T. Jackowski, et al., Chem. Rev. 120 (2020) 5437–5516.
[18] F. Wang, X. Xu, J. Mao, Diam. Relat. Mater. 109 (2020) 108037.
[19] S. Giddey, S.P.S. Badwal, A. Kulkarni, Int. J. Hydrog. Energy 38 (2013) 14576–14594.
[20] M. Jin, X. Zhang, M. Han, et al., J. Mater. Chem. A 8 (2020) 5936–5942.
[21] Q. Wang, Y. Lei, D. Wang, et al., Energy Environ. Sci. 12 (2019) 1730–1750.
[22] W. Tong, B. Huang, P. Wang, et al., Natl. Sci. Rev. 8 (2021) nwaa088.
[23] L. Wang, M. Wu, X. Lang, et al., ChemCatChem 12 (2020) 3937–3945.
[24] M. Li, H. Huang, J. Low, et al., Small Methods 3 (2019) 1800388.
[25] B. Liu, B. He, H.Q. Peng, et al., Adv. Sci. 5 (2018) 1800406.
[26] H. Wang, H. Yu, Z. Wang, et al., Small 15 (2019) 1804769.
[27] A. Liu, Y. Yang, D. Kong, et al., Appl. Surf. Sci. 536 (2021) 147851.
[28] B. Fan, H. Wang, H. Zhang, et al., Adv. Funct. Mater. 32 (2022) 2110783.
[29] C. Xie, D. Yan, W. Chen, et al., Mater. Today 31 (2019) 47–68.
[30] Y. Wang, M.M. Shi, D. Bao, et al., Angew. Chem. Int. Ed. 58 (2019) 9464–9469.
[31] V. Sorkin, Y. Cai, Z. Ong, et al., Crit. Rev. Solid State Mater. Sci. 42 (2017) 1–82.
[32] S. Qiao, Q. Wang, D. Lei, et al., J. Mater. Chem. A 10 (2022) 11702–11711.
[33] Z. Zhang, X. Liu, D. Wang, et al., Chem. Eng. J. 446 (2022) 137037.
[34] Y. Zhang, J. Lu, L. Zhang, et al., Appl. Catal. B 309 (2022) 121249.
[35] X. Zhang, C. Wang, Y. Guo, et al., J. Mater. Chem. A 10 (2022) 6448–6453.
[36] M. Li, X. Wu, K. Liu, et al., J. Energy Chem. 69 (2022) 506–515.
[37] Y. Zhu, Y. Sun, J. Khan, et al., Chem. Eng. J. 443 (2022) 136501.
[38] L. Wu, P. Guo, X. Wang, et al., Chem. Eng. J. 446 (2022) 136759.
[39] T. Tian, X. Jin, N. Guo, et al., Appl. Catal. B 308 (2022) 121227.
[40] Y. Fang, Y. Xue, L. Hui, et al., Adv. Sci. 9 (2022) 2102721.
[41] M. Yarali, H. Brahmi, Z. Yan, et al., ACS Appl. Mater. Interfaces 10 (2018) 4921–4928.
[42] Y. Kou, K. Wang, M. Wumaer, et al., Appl. Surf. Sci. 589 (2022) 153031.
[43] I.E. Khalil, C. Xue, W. Liu, et al., Adv. Funct. Mater. 31 (2021) 2010052.
[44] X. Guo, W. Ye, Z.A. Chen, et al., Appl. Catal. B 310 (2022) 121334.
[45] Z. Chen, J. Cao, X. Wu, et al., ACS Appl. Mater. Interfaces 14 (2022) 12223–12233.
[46] H.J. Liu, C.Y. Chiang, Y.S. Wu, et al., ACS Catal. 12 (2022) 6132–6142.
[47] C. Yan, W. Luo, H. Yuan, et al., Appl. Catal. B 308 (2022) 121191.
[48] Y. Zou, J. Hu, B. Li, et al., Appl. Catal. B 312 (2022) 121408.
[49] K. Li, W. Cai, Z. Zhang, et al., Chem. Eng. J. 435 (2022) 135017.
[50] T. Ma, H. Cao, S. Li, et al., Adv. Mater. 33 (2022) 2206368.
[51] X. Wang, L. Yu, B.Y. Guan, et al., Adv. Mater. 30 (2018) 1801211.
[52] L. Xu, Y. Zou, Z. Xiao, et al., J. Energy Chem. 35 (2019) 24–29.
[53] R. Grantab, V.B. Shenoy, R.S. Ruoff, Science 330 (2010) 946–948.
[54] H. Liu, X.M. Wang, H. Liang, et al., Int. J. Solids Struct. 191-192 (2020) 464–472.
[55] Y. Kang, H. Du, B. Jiang, et al., J. Mater. Chem. A 10 (2022) 6560–6568.
[56] Z. Wu, T. Wang, J.J. Zou, et al., ACS Catal. 12 (2022) 5911–5920.
[57] R. Shi, Y. Zhao, G.I.N. Waterhouse, et al., ACS Catal. 9 (2019) 9739–9750.
[58] B. Garlyyev, J. Fichtner, O. Piqué, et al., Chem. Sci. 10 (2019) 8060–8075.
[59] H. Huang, L. Chen, C. Liu, et al., J. Mater. Chem. A 4 (2016) 14577–14585.
[60] B. Jiang, T. Yang, T. Wang, et al., Chem. Eng. J. 442 (2022) 136119.
[61] C. Xue, X. Zhou, X. Li, et al., Adv. Sci. 9 (2022) 2104183.
[62] G. Chen, P. Liu, Z. Liao, et al., Adv. Mater. 32 (2020) 1907399.
[63] X. Wang, Y. Zhang, H. Si, et al., J. Am. Chem. Soc. 142 (2020) 4298–4308.
[64] X. She, X. Zhu, J. Yang, et al., Nano Energy 84 (2021) 105869.
[65] J. Ge, P. Yin, Y. Chen, et al., Adv. Mater. 33 (2021) 2006711.
[66] G. Li, K. He, F. Zhang, et al., Appl. Catal. B 309 (2022) 121231.
[67] X. Wan, W. Guo, X. Dong, et al., Green Chem. 24 (2022) 1090–1095.
[68] M. Jiang, A. Tao, Y. Hu, et al., ACS Appl. Mater. Interfaces 14 (2022) 17470–17478.

[69] Y. Liu, H. Cheng, M. Lyu, et al., J. Am. Chem. Soc. 136 (2014) 15670–15675.
[70] P. Li, Z. Jin, Z. Fang, et al., Energy Environ. Sci. 14 (2021) 3522–3531.
[71] W. Li, D. Wang, Y. Zhang, et al., Adv. Mater. 32 (2020) 1907879.
[72] D. Wang, Y. Zou, L. Tao, et al., Chin. Chem. Lett. 30 (2019) 826–838.
[73] L. Ma, C. Wang, B.Y. Xia, et al., Angew. Chem. Int. Ed. 54 (2015) 5666–5671.
[74] H. Rong, J. Mao, P. Xin, et al., Adv. Mater. 28 (2016) 2540–2546.
[75] X. Wang, L. Figueroa-Cosme, X. Yang, et al., Nano Lett. 16 (2016) 1467–1471.
[76] J. Zhu, Y. Huang, W. Mei, et al., Angew. Chem. Int. Ed. 58 (2019) 3859–3864.
[77] Á. Morales-García, F. Calle-Vallejo, F. Illas, ACS Catal. 10 (2020) 13487–13503.
[78] X. Wu, S. Xiao, Y. Long, et al., Small 18 (2022) 2105831.
[79] R. Meshkian, M. Dahlqvist, J. Lu, et al., Adv. Mater. 30 (2018) 1706409.
[80] M. Ma, X. Han, H. Li, et al., Appl. Catal. B 265 (2020) 118568.
[81] S. Dou, L. Tao, J. Huo, et al., Energy Environ. Sci. 9 (2016) 1320–1326.
[82] B. Ma, S. Ren, P. Wang, et al., Nano Res. 12 (2019) 137–142.
[83] Y. Tian, Z. Wei, X. Wang, et al., Int. J. Hydrog. Energy 42 (2017) 4184–4192.
[84] L. Zhang, X.Y. Xie, H. Wang, et al., Chem. Commun. 55 (2019) 4627–4630.
[85] F. Guo, P. Yang, Z. Pan, et al., Angew. Chem. Int. Ed. 56 (2017) 8231–8235.
[86] B. Zhang, Y. Zheng, T. Ma, et al., Adv. Mater. 33 (2021) 2006042.
[87] Y.N. Gong, L. Jiao, Y. Qian, et al., Angew. Chem. Int. Ed. 59 (2020) 2705–2709.
[88] S. Chen, H. Jang, J. Wang, et al., J. Mater. Chem. A 8 (2020) 2099–2104.
[89] R. Anwar, N. Iqbal, S. Hanif, et al., Catalysts 10 (2020) 799.
[90] C. Young, J. Wang, J. Kim, et al., Chem. Mater. 30 (2018) 3379–3386.
[91] N. Bhuvanendran, S. Ravichandran, S. Kandasamy, et al., Int. J. Hydrog. Energy 46 (2021) 2128–2142.
[92] J. Wang, X. Xiao, Y. Liu, et al., J. Mater. Chem. A 7 (2019) 17675–17702.
[93] C. Chen, D. Yan, Y. Wang, et al., Small 15 (2019) 1805029.
[94] Y. Wang, Y. Tian, J. Zhang, et al., ACS Appl. Energy Mater. 3 (2020) 9516–9522.
[95] J. Mao, Y. Chen, J. Pei, et al., Chem. Commun. 52 (2016) 5985–5988.
[96] X. Yang, Y. Ma, Y. Liu, et al., ACS Appl. Mater. Interfaces 13 (2021) 19864–19872.
[97] X. Wang, Z. Feng, B. Xiao, et al., Green Chem. 22 (2020) 6157–6169.
[98] H. Liao, X. Guo, Y. Hou, et al., Small 16 (2020) 1905223.
[99] J. Han, Z. Liu, Y. Ma, et al., Nano Energy 52 (2018) 264–270.
[100] Y. Liu, C. Xiao, Z. Li, et al., Adv. Energy Mater. 6 (2016) 1600436.
[101] X. Wang, X. Gan, T. Hu, et al., Adv. Mater. 29 (2017) 1603617.
[102] Z. Cai, Y. Bi, E. Hu, et al., Adv. Energy Mater. 8 (2018) 1701694.
[103] Y. Zhao, Y. Zhao, R. Shi, et al., Adv. Mater. 31 (2019) 1806482.
[104] Y. Zhang, C. Zhang, Y. Guo, et al., J. Mater. Chem. A 7 (2019) 2536–2540.
[105] S. Dou, X. Wang, S. Wang, Small Methods 3 (2019) 1800211.
[106] B.K. Sharma, A. Stoesser, S.K. Mondal, et al., ACS Appl. Mater. Interfaces 10 (2018) 22408–22418.
[107] S. Gao, Z. Sun, W. Liu, et al., Nat. Commun. 8 (2017) 14503.
[108] X. Yao, J. Liu, W. Wang, et al., J. Chem. Phys. 146 (2017) 224703.
[109] J. Kim, X. Yin, K.C. Tsao, et al., J. Am. Chem. Soc. 136 (2014) 14646–14649.
[110] S. Choi, Y. Park, H. Yang, et al., CrystEngComm 22 (2020) 1500–1513.
[111] T. Ling, D.Y. Yan, Y. Jiao, et al., Nat. Commun. 7 (2016) 12876.
[112] C. Lv, C. Yan, G. Chen, et al., Angew. Chem. Int. Ed. 57 (2018) 6073–6076.
[113] W. Fu, P. Zhuang, M.O.L. Chee, et al., ACS Sustain. Chem. Eng. 7 (2019) 9622–9628.
[114] Y. Fang, Z. Liu, J. Han, et al., Adv. Energy Mater. 9 (2019) 1803406.
[115] J. Zhang, Y. Ji, P. Wang, et al., Adv. Funct. Mater. 30 (2020) 1906579.
[116] Y. Liu, X. Kong, X. Guo, et al., ACS Catal. 10 (2020) 1077–1085.
[117] C. Fang, T. Bi, X. Xu, et al., Adv. Mater. Interfaces 6 (2019) 1901034.
[118] C. Zhang, S. Liu, T. Chen, et al., Chem. Commun. 55 (2019) 7370–7373.
[119] S. Cheng, Y.J. Gao, Y.L. Yan, et al., J. Energy Chem. 39 (2019) 144–151.
[120] Z. Han, C. Choi, S. Hong, et al., Appl. Catal. B 257 (2019) 117896.
[121] Y. Abghoui, A.L. Garden, V.F. Hlynsson, et al., Phys. Chem. Chem. Phys. 17 (2015) 4909–4918.
[122] Y. Abghoui, A.L. Garden, J.G. Howalt, et al., ACS Catal. 6 (2016) 635–646.
[123] Q. Li, L. He, C. Sun, et al., J. Phys. Chem. C 121 (2017) 27563–27568.
[124] C. Lv, Y. Qian, C. Yan, et al., Angew. Chem. Int. Ed. 57 (2018) 10246–10250.
[125] H. Jin, L. Li, X. Liu, et al., Adv. Mater. 31 (2019) 1902709.
[126] X. Li, T. Li, Y. Ma, et al., Adv. Energy Mater. 8 (2018) 1801357.
[127] L. Zhang, X. Ji, X. Ren, et al., Adv. Mater. 30 (2018) 1800191.
[128] J. Zhang, X. Tian, M. Liu, et al., J. Am. Chem. Soc. 141 (2019) 19269–19275.
[129] B.H.R. Suryanto, D. Wang, L.M. Azofra, et al., ACS Energy Lett. 4 (2019) 430–435.
[130] L.M. Azofra, C. Sun, L. Cavallo, et al., Chem. Eur. J. 23 (2017) 8275–8279.
[131] H. Zhang, C. Cui, Z. Luo, J. Phys. Chem. C 124 (2020) 6260–6266.
[132] W. Zhang, B.W. Zhang, Nanomicro Lett. 13 (2021) 106.
[133] X. Yan, Y. Jia, X. Yao, Chem. Soc. Rev. 47 (2018) 7628–7658.
[134] C. Zhu, S. Fu, Q. Shi, et al., Angew. Chem. Int. Ed. 56 (2017) 13944–13960.
[135] Z. Wei, Y. Zhang, S. Wang, et al., J. Mater. Chem. A 6 (2018) 13790–13796.
[136] C. Choi, S. Back, N.Y. Kim, et al., ACS Catal. 8 (2018) 7517–7525.
[137] X. Chen, X. Zhao, Z. Kong, et al., J. Mater. Chem. A 6 (2018) 21941–21948.
[138] W. Yang, H. Huang, X. Ding, et al., Electrochim. Acta 335 (2020) 135667.
[139] C. Guo, X. Liu, L. Gao, et al., Appl. Catal. B 263 (2020) 118296.
[140] F. Lai, N. Chen, X. Ye, et al., Adv. Funct. Mater. 30 (2020) 1907376.
[141] Y. Shi, Y. Zhou, D.R. Yang, et al., J. Am. Chem. Soc. 139 (2017) 15479–15485.
[142] J. Su, R. Ge, Y. Dong, et al., J. Mater. Chem. A 6 (2018) 14025–14042.
[143] Y. Zhang, L. Guo, L. Tao, et al., Small Methods 3 (2019) 1800406.
[144] X. Yang, K. Li, D. Cheng, et al., J. Mater. Chem. A 6 (2018) 7762–7769.
[145] H. Wang, L. Wang, Q. Wang, et al., Angew. Chem. Int. Ed. 57 (2018) 12360–12364.
[146] X. Yu, P. Han, Z. Wei, et al., Joule 2 (2018) 1610–1622.
[147] X. Mao, S. Zhou, C. Yan, et al., Phys. Chem. Chem. Phys. 21 (2019) 1110–1116.
[148] Y. Tian, D. Xu, K. Chu, et al., J. Mater. Sci. 54 (2019) 9088–9097.
[149] J.S. Kim, B. Kim, H. Kim, et al., Adv. Energy Mater. 8 (2018) 1702774.
[150] J. Zhang, R. Yin, Q. Shao, et al., Angew. Chem. Int. Ed. 58 (2019) 5609–5613.
[151] W. Xu, S. Zhu, Y. Liang, et al., J. Mater. Chem. A 5 (2017) 18793–18800.
[152] P. Cai, J. Huang, J. Chen, et al., Angew. Chem. Int. Ed. 56 (2017) 4858–4861.
[153] S.J. Li, D. Bao, M.M. Shi, et al., Adv. Mater. 29 (2017) 1700001.
[154] Z. Wang, Y. Li, H. Yu, et al., ChemSusChem 11 (2018) 3480–3485.
[155] M.M. Shi, D. Bao, B.R. Wulan, et al., Adv. Mater. 29 (2017) 1606550.
[156] H. Yu, Z. Wang, W. Tian, et al., Mater. Today Energy 20 (2021) 100681.
[157] R. Lan, J.T.S. Irvine, S. Tao, Sci. Rep. 3 (2013) 1145.
[158] M. Kitano, S. Kanbara, Y. Inoue, et al., Nat. Commun. 6 (2015) 6731.
[159] M.M. Shi, D. Bao, S.J. Li, et al., Adv. Energy Mater. 8 (2018) 1800124.
[160] C. Guo, J. Ran, A. Vasileff, et al., Energy Environ. Sci. 11 (2018) 45–56.
[161] P. Li, W. Fu, P. Zhuang, et al., Small 15 (2019) 1902535.
[162] P. De Luna, W. Liang, A. Mallick, et al., ACS Appl. Mater. Interfaces 10 (2018) 31225–31232.
[163] Y. Song, D. Johnson, R. Peng, et al., Sci. Adv. 4 (2018) e1700336.
[164] W.Y. Gao, Y.C. Hao, X. Su, et al., Chem. Commun. 55 (2019) 10705–10708.
[165] H. Ying, T. Chen, C. Zhang, et al., J. Colloid Interface Sci. 602 (2021) 64–72.
[166] H. Wang, H. Yu, Y. Li, et al., Nanotechnology 29 (2018) 175403.
[167] H. Yu, Z. Wang, D. Yang, et al., J. Mater. Chem. A 7 (2019) 12526–12531.
[168] F. Pang, Z. Wang, K. Zhang, et al., Nano Energy 58 (2019) 834–841.
[169] F. Lai, W. Zong, G. He, et al., Angew. Chem. Int. Ed. 59 (2020) 13320–13327.
[170] B. Xu, L. Xia, F. Zhou, et al., ACS Sustain. Chem. Eng. 7 (2019) 2889–2893.
[171] C. Ma, N. Zhai, B. Liu, et al., Electrochim. Acta 370 (2021) 137695.
[172] L. Wen, X. Li, R. Zhang, et al., ACS Appl. Mater. Interfaces 13 (2021) 14181–14188.
[173] G. Zhang, Q. Ji, K. Zhang, et al., Nano Energy 59 (2019) 10–16.
[174] L. Yang, T. Wu, R. Zhang, et al., Nanoscale 11 (2019) 1555–1562.
[175] K. Chu, F. Liu, J. Zhu, et al., Adv. Energy Mater. 11 (2021) 2003799.
[176] Z. Sun, R. Huo, C. Choi, et al., Nano Energy 62 (2019) 869–875.
[177] J. Xia, H. Guo, M. Cheng, et al., J. Mater. Chem. A 9 (2021) 2145–2151.
[178] X. Yang, F. Ling, J. Su, et al., Appl. Catal. B 264 (2020) 118477.
[179] W. Zang, T. Yang, H. Zou, et al., ACS Catal. 9 (2019) 10166–10173.
[180] X.W. Lv, X.L. Liu, L.J. Gao, et al., J. Mater. Chem. A 9 (2021) 4026–4035.
[181] S. Xiao, F. Luo, H. Hu, et al., Chem. Commun. 56 (2020) 446–449.
[182] T. Wu, H. Zhao, X. Zhu, et al., Adv. Mater. 32 (2020) 2000299.
[183] T. Wu, X. Li, X. Zhu, et al., Chem. Commun. 56 (2020) 1831–1834.
[184] W. Peng, M. Luo, X. Xu, et al., Adv. Energy Mater. 10 (2020) 2001364.
[185] K. Chu, Y.P. Liu, Y.B. Li, et al., Appl. Catal. B 264 (2020) 118525.
[186] H. Chen, Y. Xiao, C. Chen, et al., ACS Appl. Mater. Interfaces 11 (2019) 11459–11465.
[187] S. Zhao, H.X. Liu, Y. Qiu, et al., J. Mater. Chem. A 8 (2020) 6586–6596.
[188] X. Wang, W. Wang, M. Qiao, et al., Sci. Bull. 63 (2018) 1246–1253.
[189] K. Chu, H. Nan, Q. Li, et al., J. Energy Chem. 53 (2021) 132–138.
[190] T. Pan, L. Wang, Y. Shen, et al., ACS Appl. Mater. Interfaces 14 (2022) 14474–14481.
[191] Y. Liu, W. Wang, S. Zhang, et al., ACS Sustain. Chem. Eng. 8 (2020) 2320–2326.
[192] Y. Liu, M. Han, Q. Xiong, et al., Adv. Energy Mater. 9 (2019) 1803935.
[193] H. Cheng, L.X. Ding, G.F. Chen, et al., Adv. Mater. 30 (2018) 1803694.
[194] H. Sun, H.Q. Yin, W. Shi, et al., Nano Res. 15 (2022) 3026–3033.
[195] Z. Wang, J. Niu, Y. Xu, et al., ACS Sustain. Chem. Eng. 8 (2020) 12588–12594.